Supplementary Material - A global re-analysis of regionally resolved emissions and atmospheric mole fractions of SF_6 for the period 2005-2021

Martin Vojta[1], Andreas Plach[1], Saurabh Annadate[2,3], Sunyong Park[4], Gawon Lee[4], Pallav Purohit[6], Florian Lindl[6], Xin Lan[8], Jens Mühle[7], Rona L. Thompson[5], and Andreas Stohl[1]

[1]Department of Meteorology and Geophysics, University of Vienna, Vienna, Austria
[2]Department of Pure and Applied Sciences, University of Urbino "Carlo Bo", Urbino, Italy
[3]University School for Advanced Studies IUSS, 27100 Pavia, Italy
[4]Kyungpook National University, Department of Oceanography, School of Earth System Sciences, Daegu, South Korea
[5]NILU, Kjeller, Norway
[6]International Institute for Applied Systems Analysis (IIASA), Laxenburg, Austria
[7]Scripps Institution of Oceanography, University of California, San Diego, CA, 92037, USA
[8]NOAA Global Monitoring Laboratory, Boulder, CO, USA
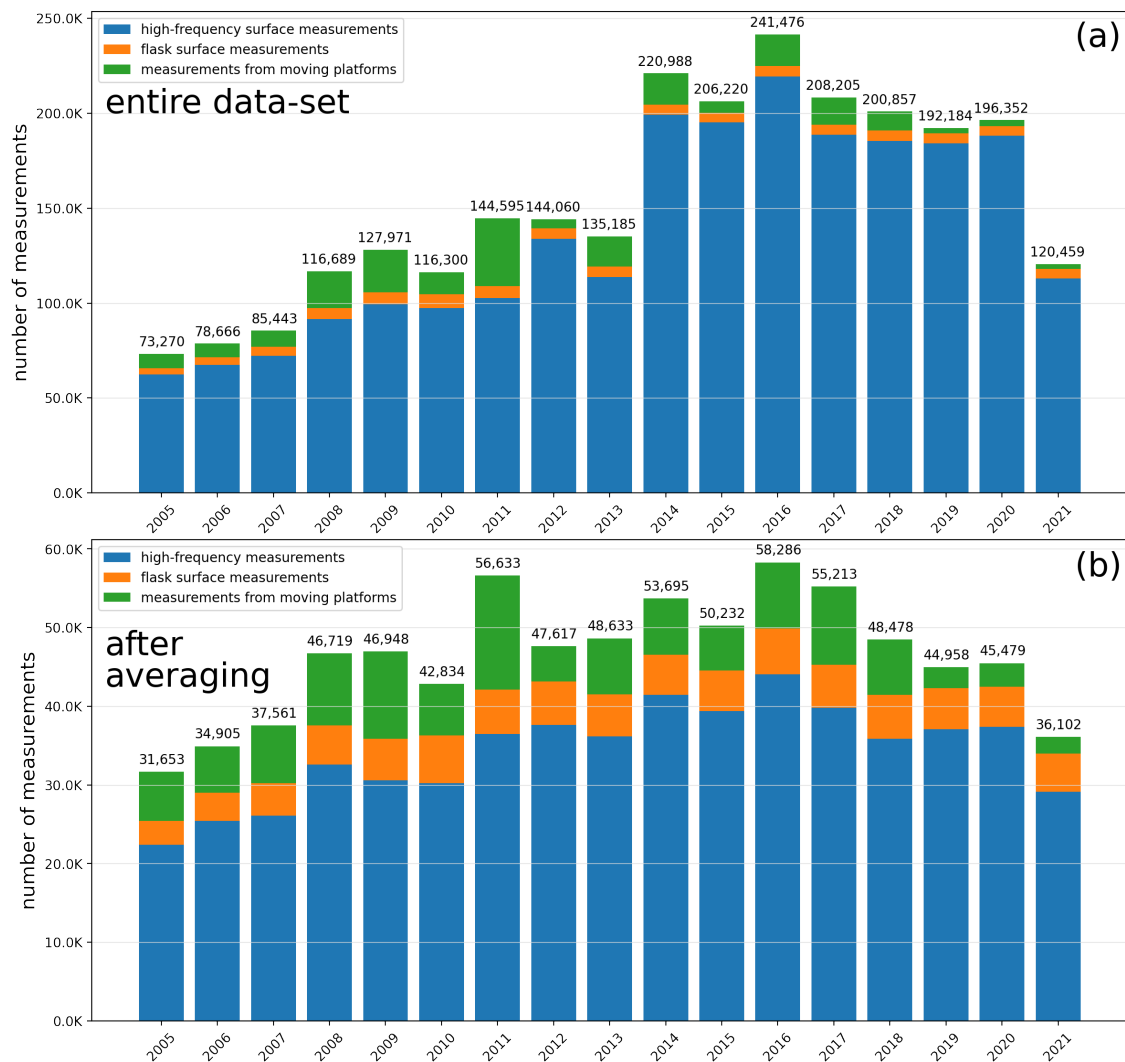
Figure S1. The total number of annual available observations of (a) the entire measurement dataset and (b) the dataset after averaging. The different colors indicate the different measurement types; blue: continuous, high-frequency surface measurements; orange: flask surface measurements; green: measurements from moving platforms.
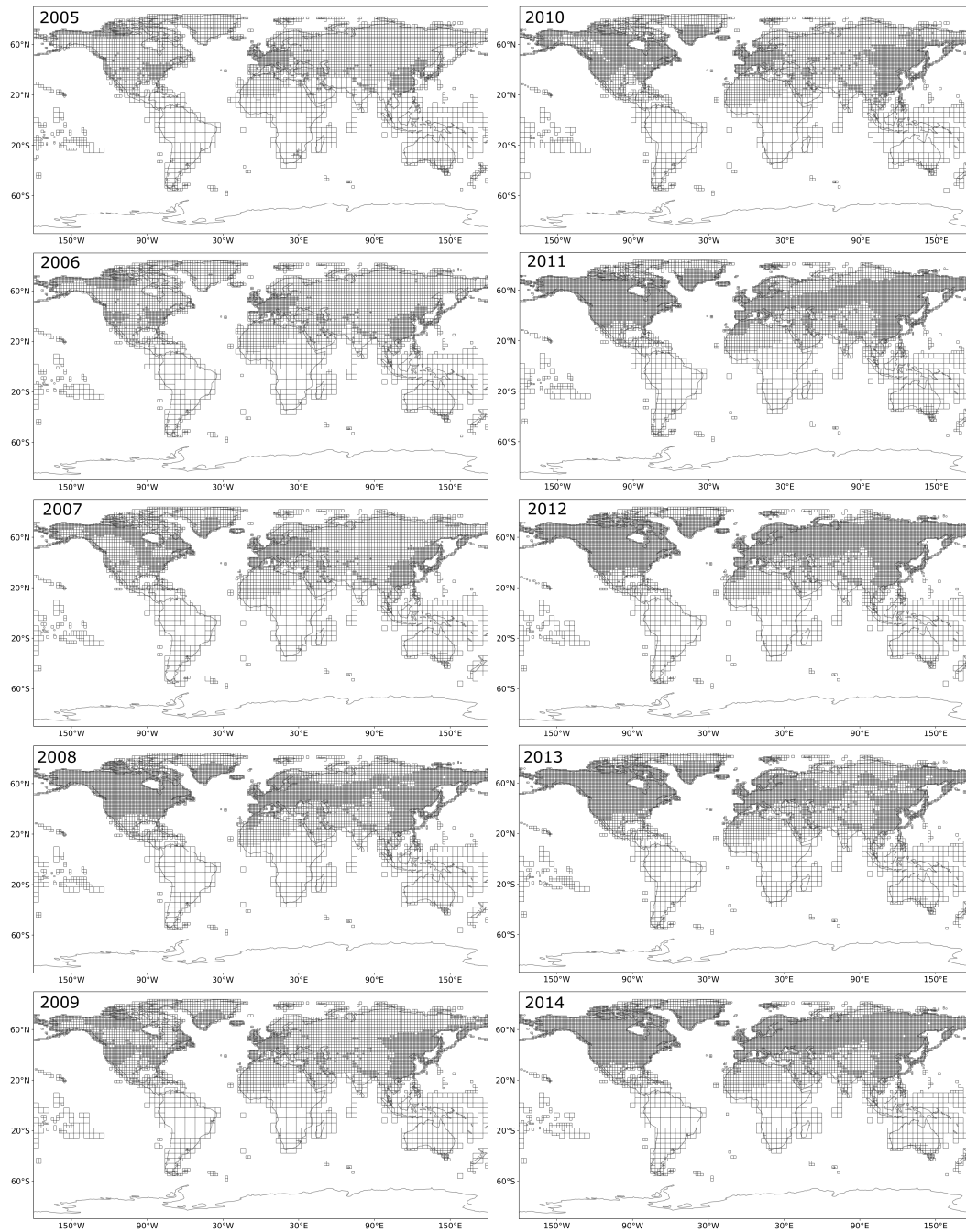
Figure S2. Global inversion grids for the years 2005 - 2014
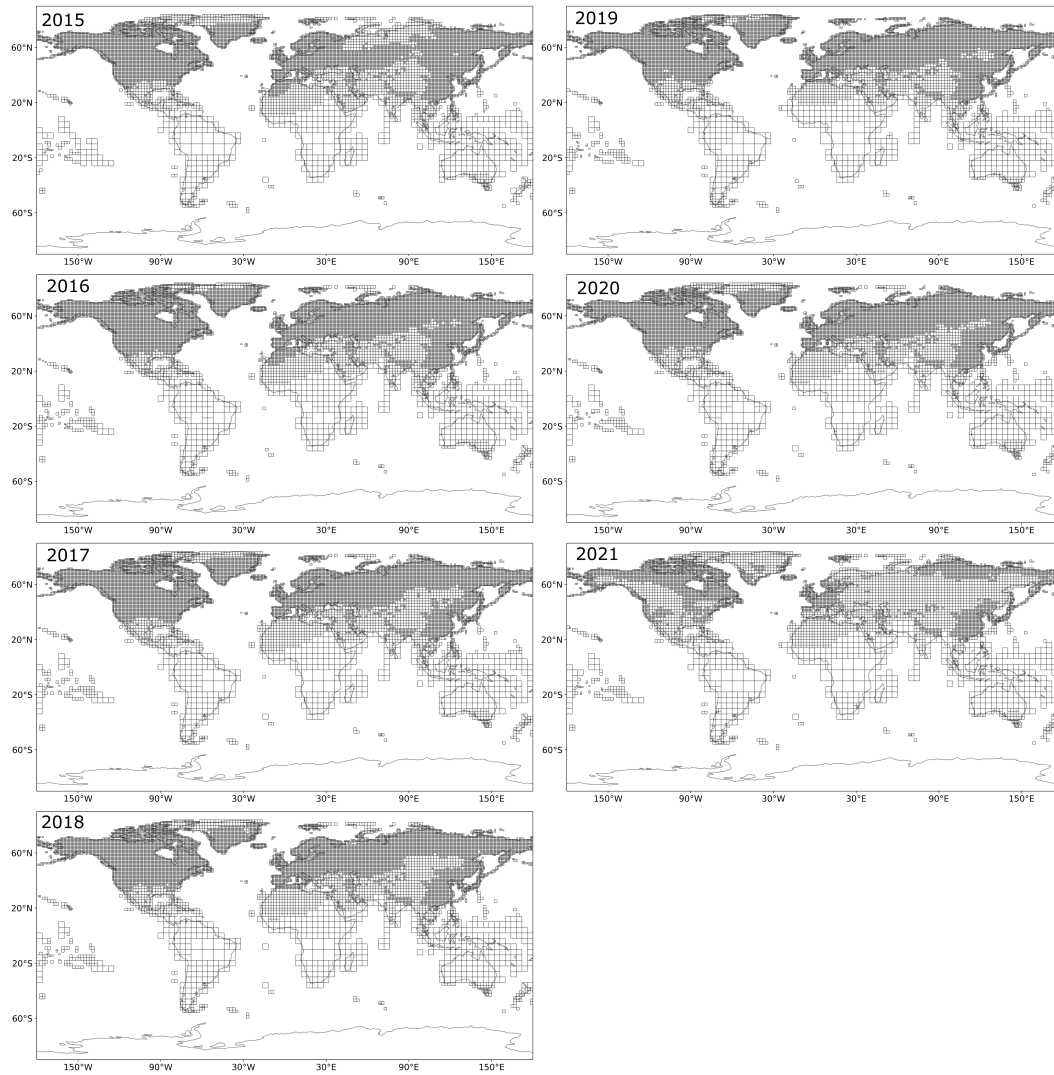
Figure S3. Global inversion grids for the years 2015 - 2021
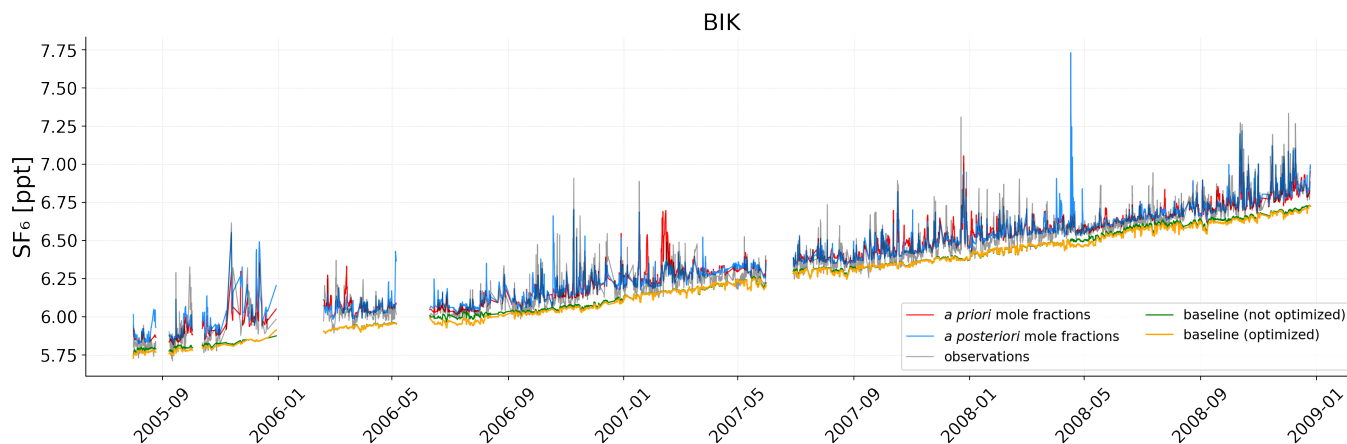
Figure S4. Mole fraction time series at the Bialystok (Poland) measurement station. Red lines illustrate the modeled *a priori* mole fractions calculated with the E7P *a priori* emissions and blue lines represent the modeled *a posteriori* mole fractions. The green line illustrates the baseline derived by the GDB method and the orange line shows the optimized baseline. The grey line represents the observed mole fractions.
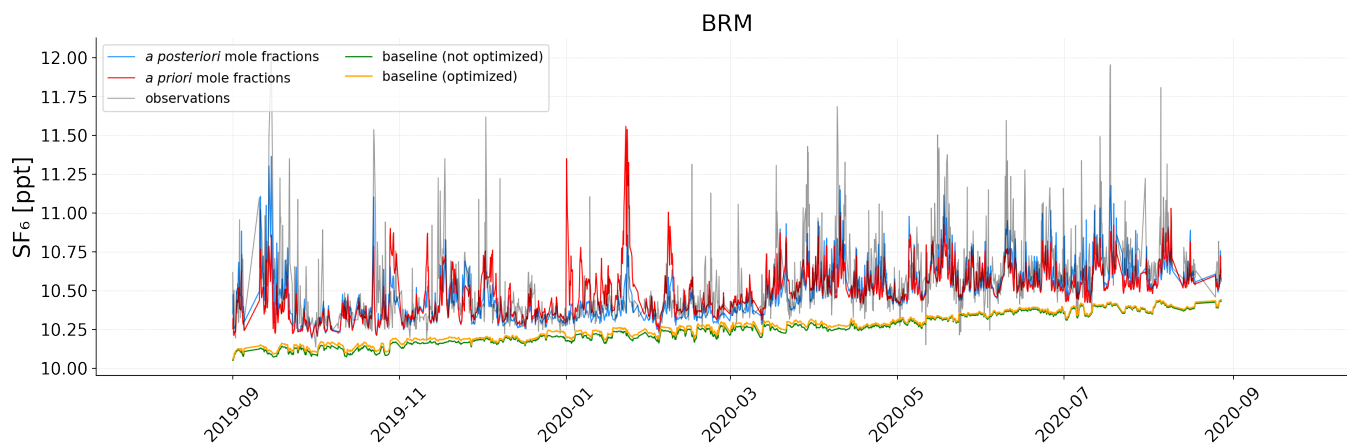
Figure S5. Mole fraction time series at the Beromünster (Switzerland) measurement station. Red lines illustrate the modeled *a priori* mole fractions calculated with the E7P *a priori* emissions and blue lines represent the modeled *a posteriori* mole fractions. The green line illustrates the baseline derived by the GDB method and the orange line shows the optimized baseline. The grey line represents the observed mole fractions.
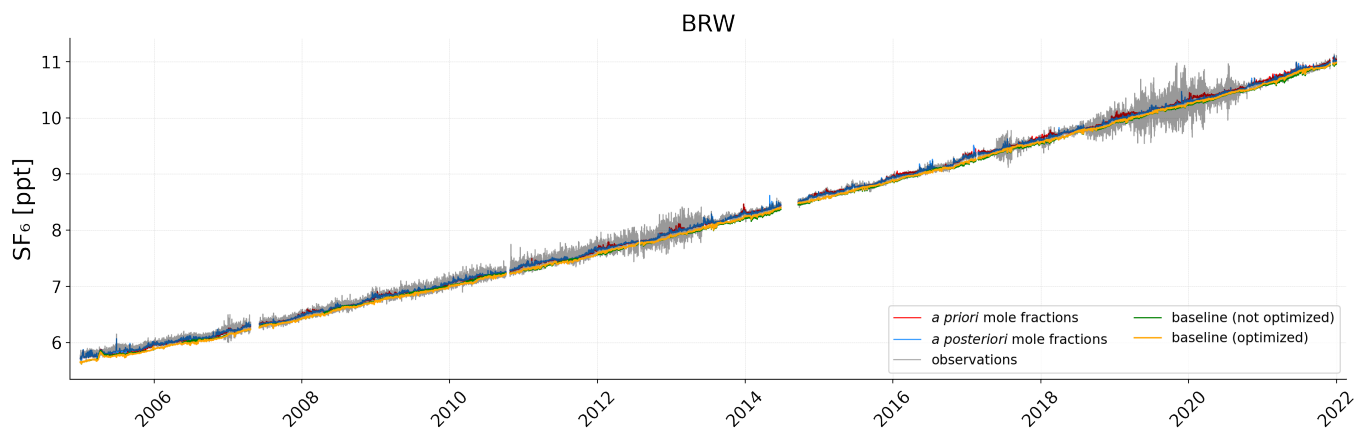
Figure S6. Mole fraction time series at the Barrow (Alaska) measurement station. Red lines illustrate the modeled *a priori* mole fractions calculated with the E7P *a priori* emissions and blue lines represent the modeled *a posteriori* mole fractions. The green line illustrates the baseline derived by the GDB method and the orange line shows the optimized baseline. The grey line represents the observed mole fractions.
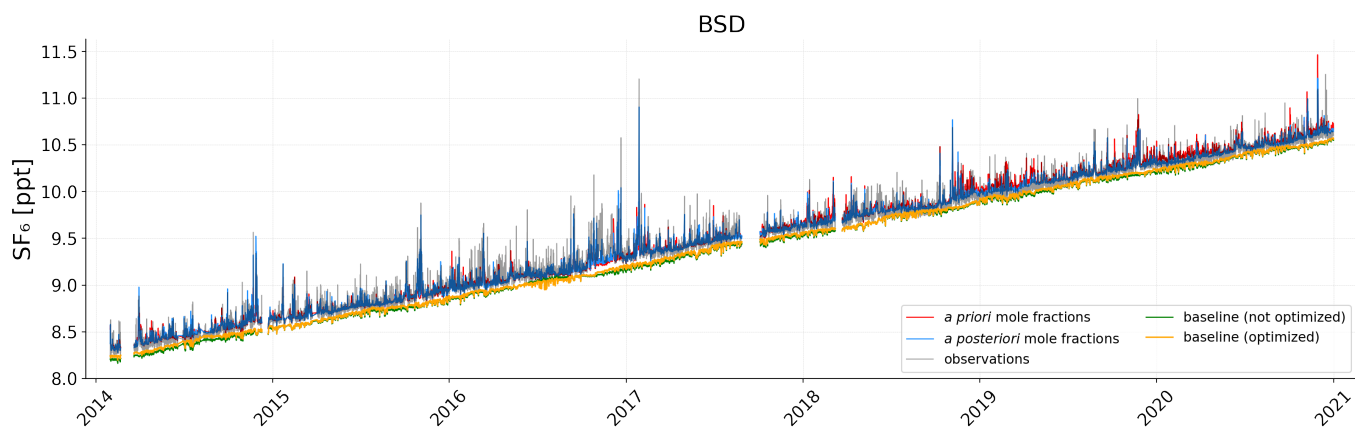
Figure S7. (a) represents the Mole fraction time series at the Bilsdale (UK) measurement station. Red lines illustrate the modeled *a priori* mole fractions calculated with the E7P *a priori* emissions and blue lines represent the modeled *a posteriori* mole fractions. The green line illustrates the baseline derived by the GDB method and the orange line shows the optimized baseline. The grey line represents the observed mole fractions.
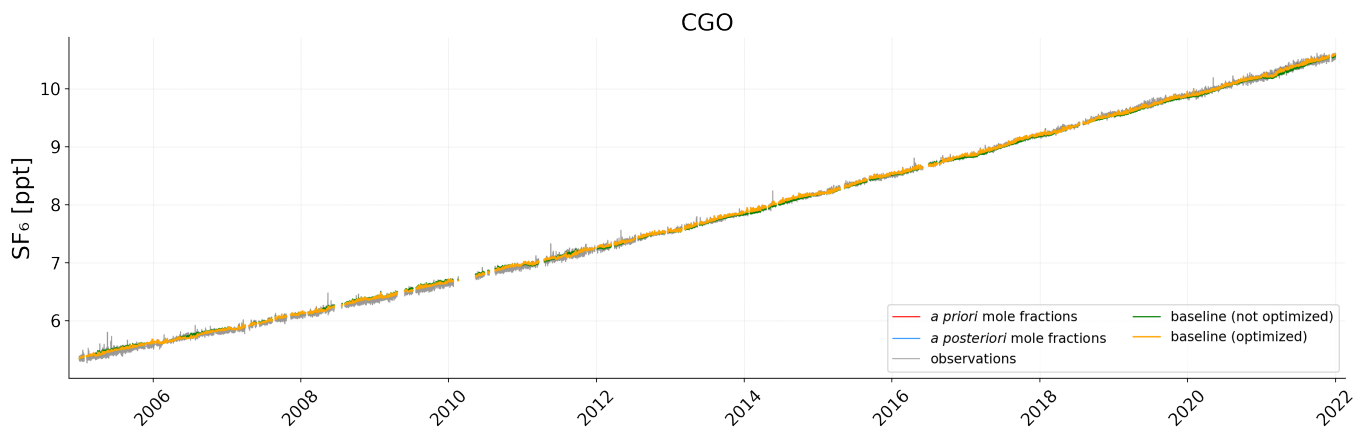
Figure S8. Mole fraction time series at the Cape Grim (Tasmania) measurement station. Red lines illustrate the modeled *a priori* mole fractions calculated with the E7P *a priori* emissions and blue lines represent the modeled *a posteriori* mole fractions. The green line illustrates the baseline derived by the GDB method and the orange line shows the optimized baseline. The grey line represents the observed mole fractions.
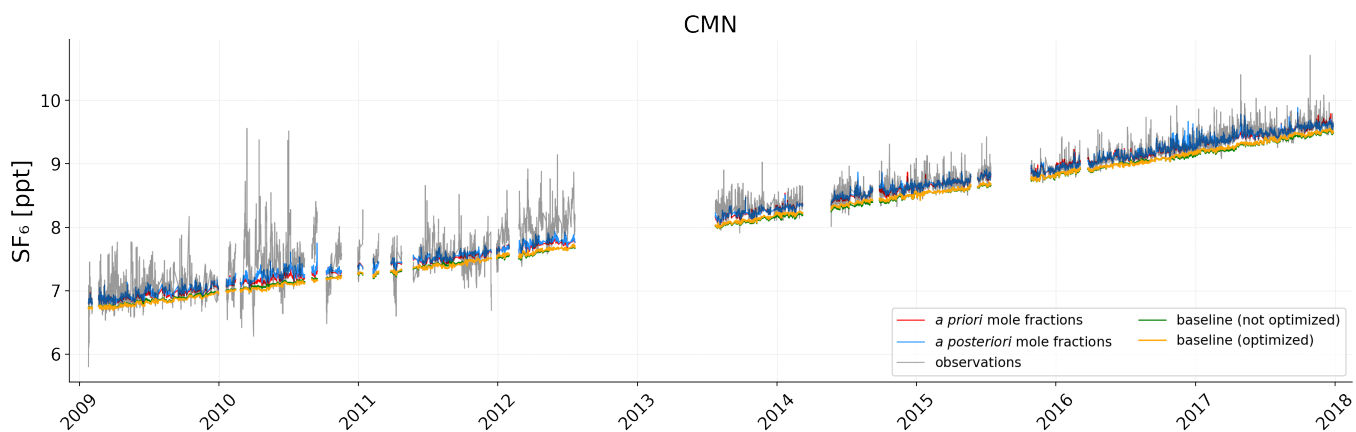
Figure S9. Mole fraction time series at the Monte Cimone (Italy) measurement station. Red lines illustrate the modeled *a priori* mole fractions calculated with the E7P *a priori* emissions and blue lines represent the modeled *a posteriori* mole fractions. The green line illustrates the baseline derived by the GDB method and the orange line shows the optimized baseline. The grey line represents the observed mole fractions.
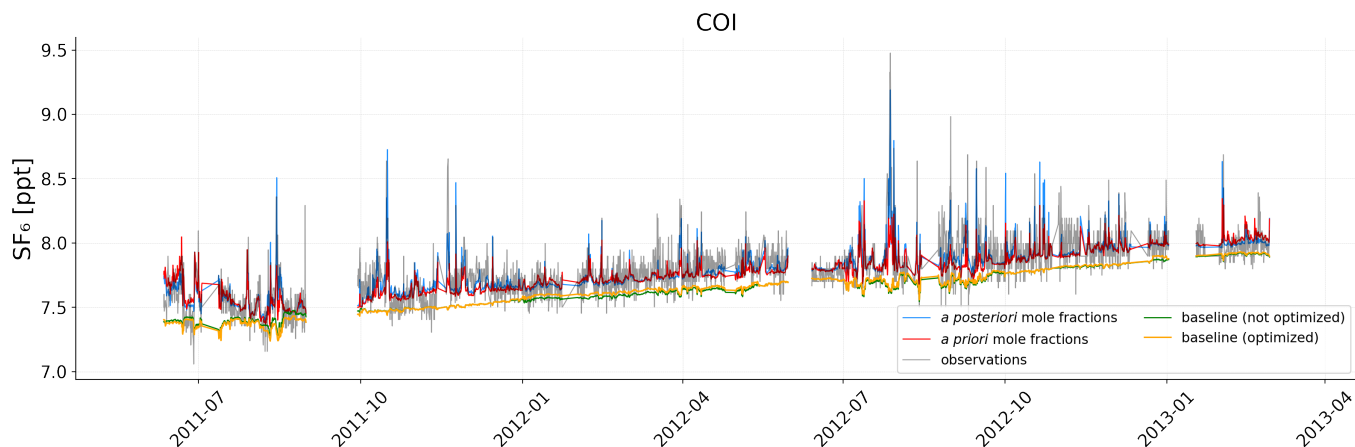
Figure S10. Mole fraction time series at the Cape Ochiishi (Japan) measurement station. Red lines illustrate the modeled *a priori* mole fractions calculated with the E7P *a priori* emissions and blue lines represent the modeled *a posteriori* mole fractions. The green line illustrates the baseline derived by the GDB method and the orange line shows the optimized baseline. The grey line represents the observed mole fractions.
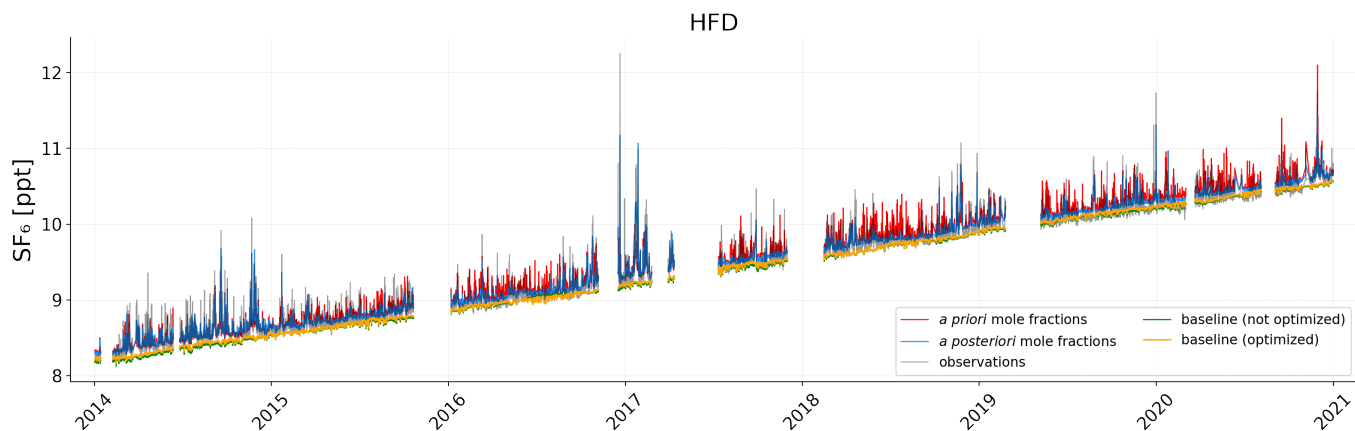
Figure S11. Mole fraction time series at the Heathfield (UK) measurement station. Red lines illustrate the modeled *a priori* mole fractions calculated with the E7P *a priori* emissions and blue lines represent the modeled *a posteriori* mole fractions. The green line illustrates the baseline derived by the GDB method and the orange line shows the optimized baseline. The grey line represents the observed mole fractions.
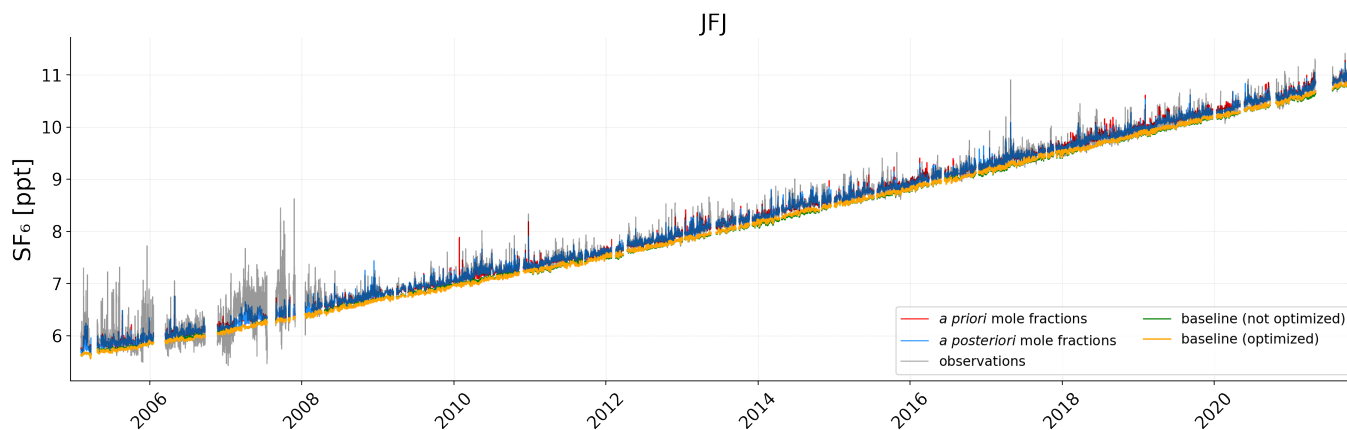
Figure S12. Mole fraction time series at the Jungfraujoch (Switzerland) measurement station. Red lines illustrate the modeled *a priori* mole fractions calculated with the E7P *a priori* emissions and blue lines represent the modeled *a posteriori* mole fractions. The green line illustrates the baseline derived by the GDB method and the orange line shows the optimized baseline. The grey line represents the observed mole fractions.
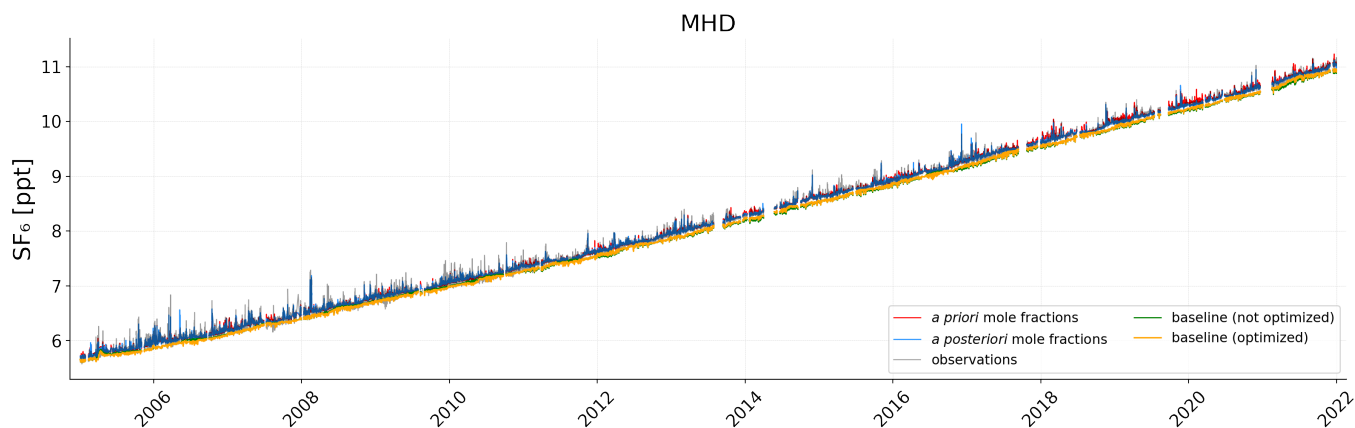
Figure S13. Mole fraction time series at the Mace Head (Ireland) measurement station. Red lines illustrate the modeled *a priori* mole fractions calculated with the E7P *a priori* emissions and blue lines represent the modeled *a posteriori* mole fractions. The green line illustrates the baseline derived by the GDB method and the orange line shows the optimized baseline. The grey line represents the observed mole fractions.
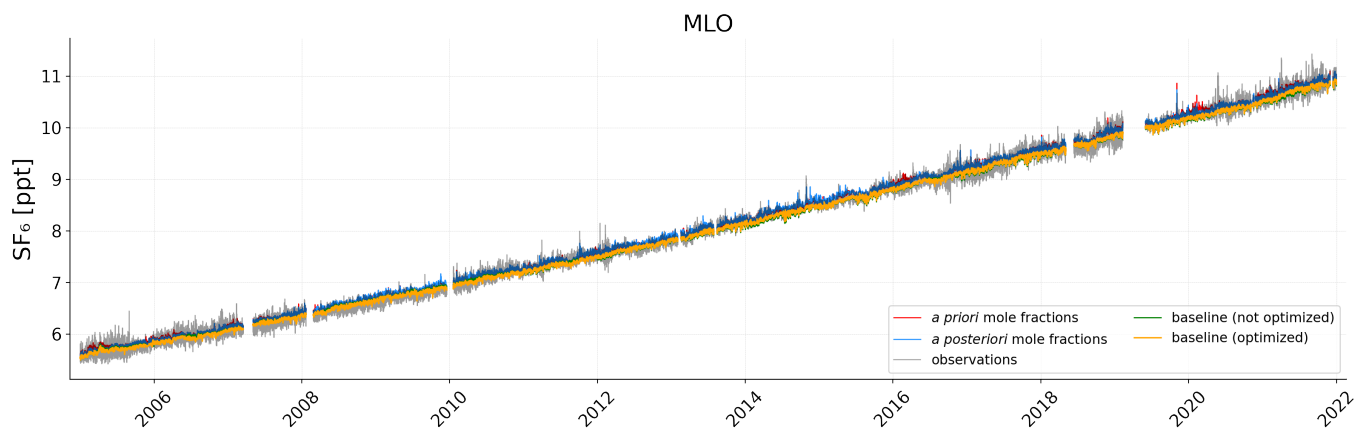
Figure S14. Mole fraction time series at the Mauna Loa (Hawaii) measurement station. Red lines illustrate the modeled *a priori* mole fractions calculated with the E7P *a priori* emissions and blue lines represent the modeled *a posteriori* mole fractions. The green line illustrates the baseline derived by the GDB method and the orange line shows the optimized baseline. The grey line represents the observed mole fractions.
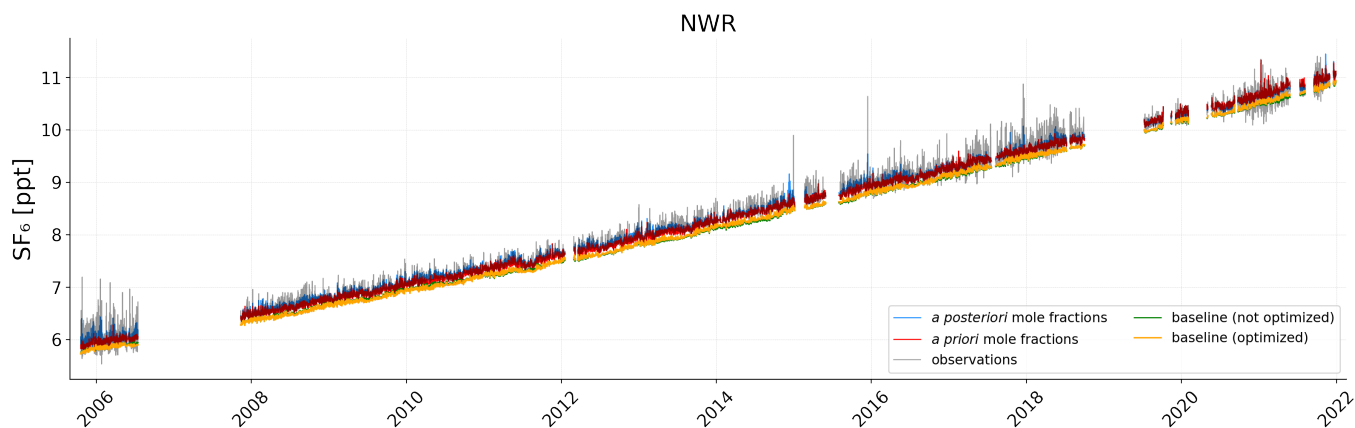
Figure S15. Mole fraction time series at the Niwot Ridge (Colorado) measurement station. Red lines illustrate the modeled *a priori* mole fractions calculated with the E7P *a priori* emissions and blue lines represent the modeled *a posteriori* mole fractions. The green line illustrates the baseline derived by the GDB method and the orange line shows the optimized baseline. The grey line represents the observed mole fractions.
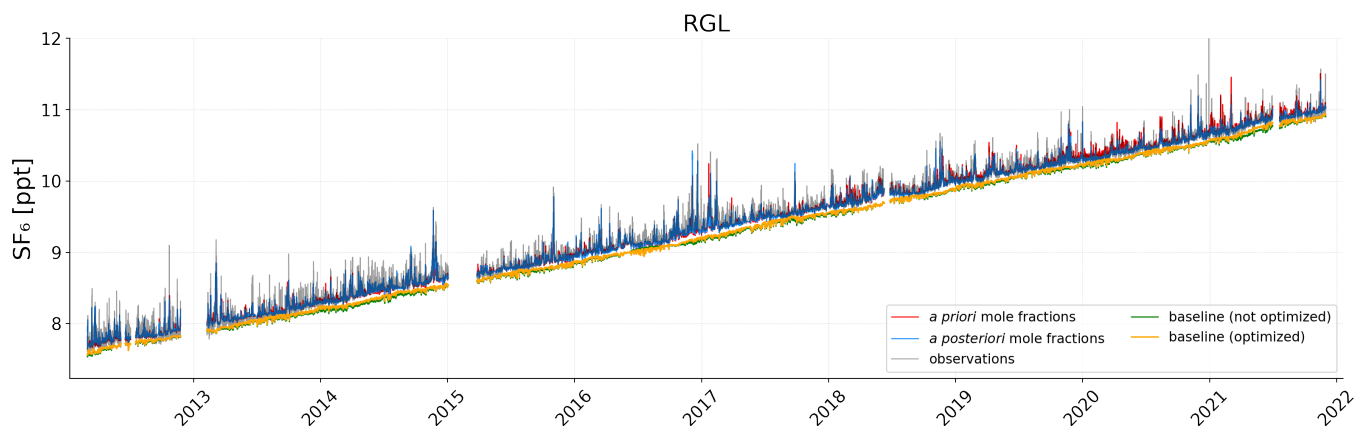
Figure S16. Mole fraction time series at the Ridge Hill (UK) measurement station. Red lines illustrate the modeled *a priori* mole fractions calculated with the E7P *a priori* emissions and blue lines represent the modeled *a posteriori* mole fractions. The green line illustrates the baseline derived by the GDB method and the orange line shows the optimized baseline. The grey line represents the observed mole fractions.
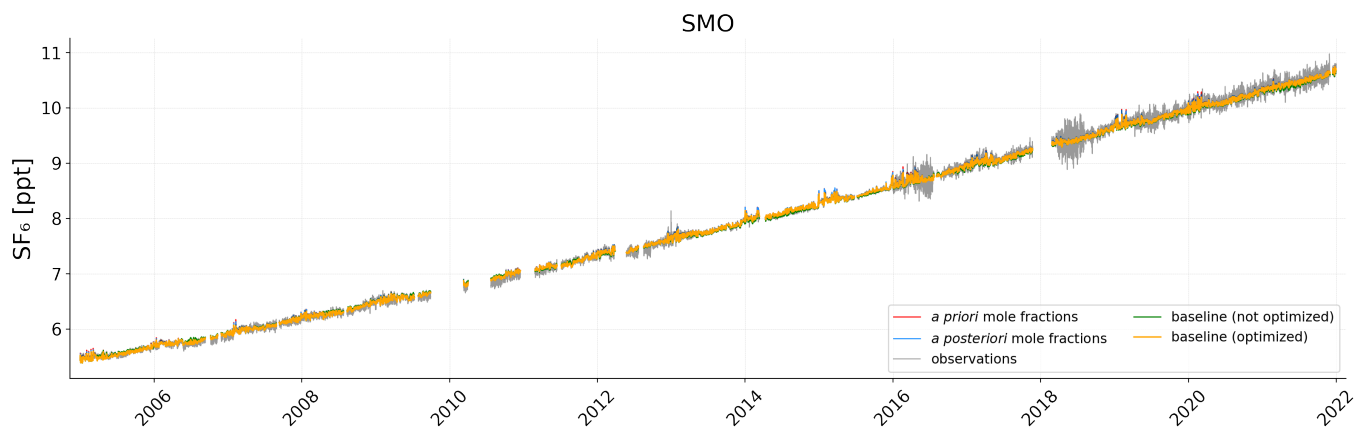
Figure S17. Mole fraction time series at the Cape Matatula (American Samoa) measurement station. Red lines illustrate the modeled *a priori* mole fractions calculated with the E7P *a priori* emissions and blue lines represent the modeled *a posteriori* mole fractions. The green line illustrates the baseline derived by the GDB method and the orange line shows the optimized baseline. The grey line represents the observed mole fractions.
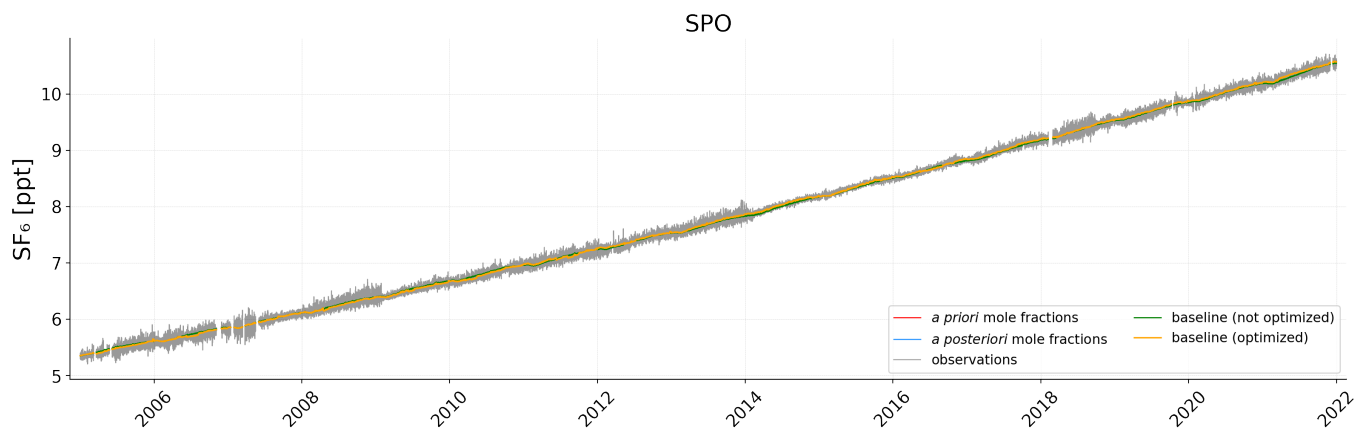
Figure S18. Mole fraction time series at the South Pole, (Antarctica) measurement station. Red lines illustrate the modeled *a priori* mole fractions calculated with the E7P *a priori* emissions and blue lines represent the modeled *a posteriori* mole fractions. The green line illustrates the baseline derived by the GDB method and the orange line shows the optimized baseline. The grey line represents the observed mole fractions.
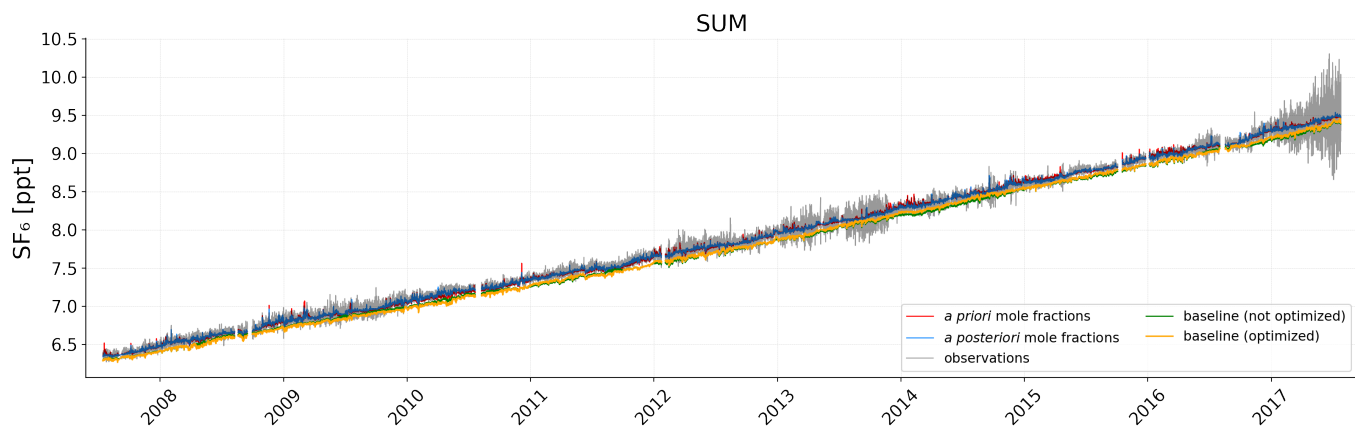
Figure S19. Mole fraction time series at the Summit (Greenland) measurement station. Red lines illustrate the modeled *a priori* mole fractions calculated with the E7P *a priori* emissions and blue lines represent the modeled *a posteriori* mole fractions. The green line illustrates the baseline derived by the GDB method and the orange line shows the optimized baseline. The grey line represents the observed mole fractions.
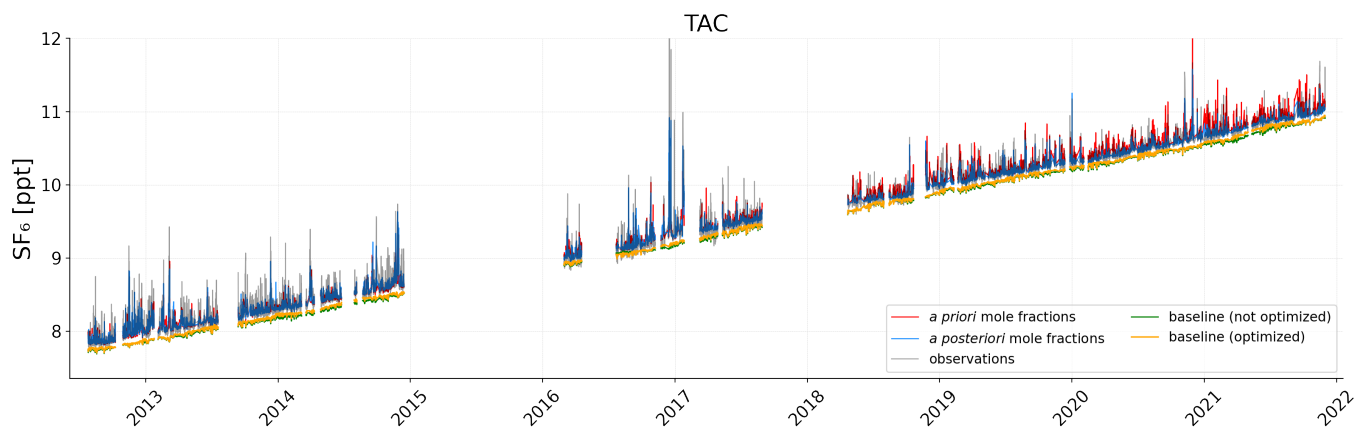
Figure S20. Mole fraction time series at the Tacolneston Tall Tower (UK) measurement station. Red lines illustrate the modeled *a priori* mole fractions calculated with the E7P *a priori* emissions and blue lines represent the modeled *a posteriori* mole fractions. The green line illustrates the baseline derived by the GDB method and the orange line shows the optimized baseline. The grey line represents the observed mole fractions.
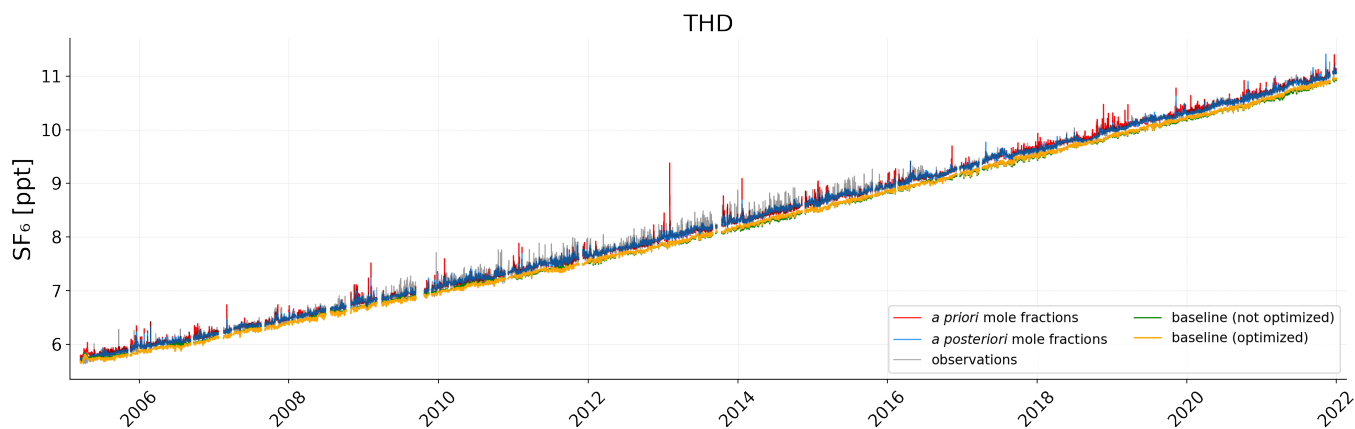
Figure S21. Mole fraction time series at the Trinidad Head (USA) measurement station. Red lines illustrate the modeled *a priori* mole fractions calculated with the E7P *a priori* emissions and blue lines represent the modeled *a posteriori* mole fractions. The green line illustrates the baseline derived by the GDB method and the orange line shows the optimized baseline. The grey line represents the observed mole fractions.
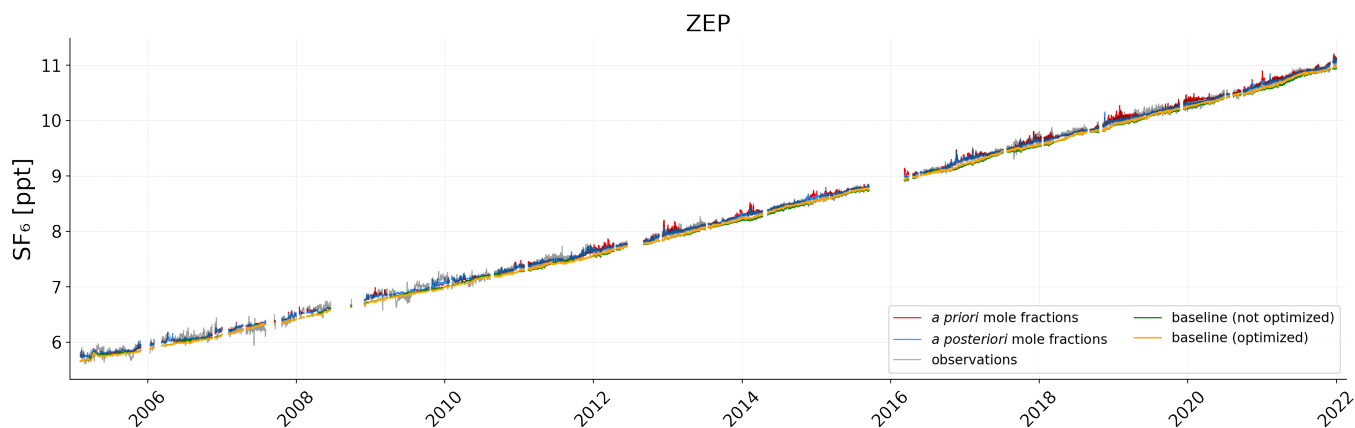
Figure S22. Mole fraction time series at the Zeppelin (Ny-Alesund, Norway) measurement station. Red lines illustrate the modeled *a priori* mole fractions calculated with the E7P *a priori* emissions and blue lines represent the modeled *a posteriori* mole fractions. The green line illustrates the baseline derived by the GDB method and the orange line shows the optimized baseline. The grey line represents the observed mole fractions.
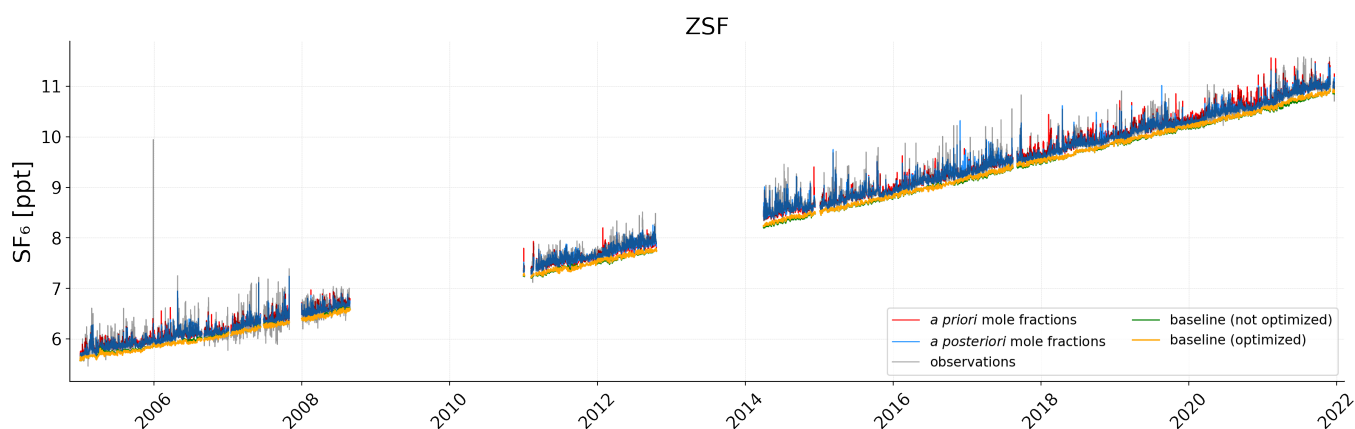
Figure S23. Mole fraction time series at the Zugspitze-Schneefernerhaus, (Germany) measurement station. Red lines illustrate the modeled *a priori* mole fractions calculated with the E7P *a priori* emissions and blue lines represent the modeled *a posteriori* mole fractions. The green line illustrates the baseline derived by the GDB method and the orange line shows the optimized baseline. The grey line represents the observed mole fractions.
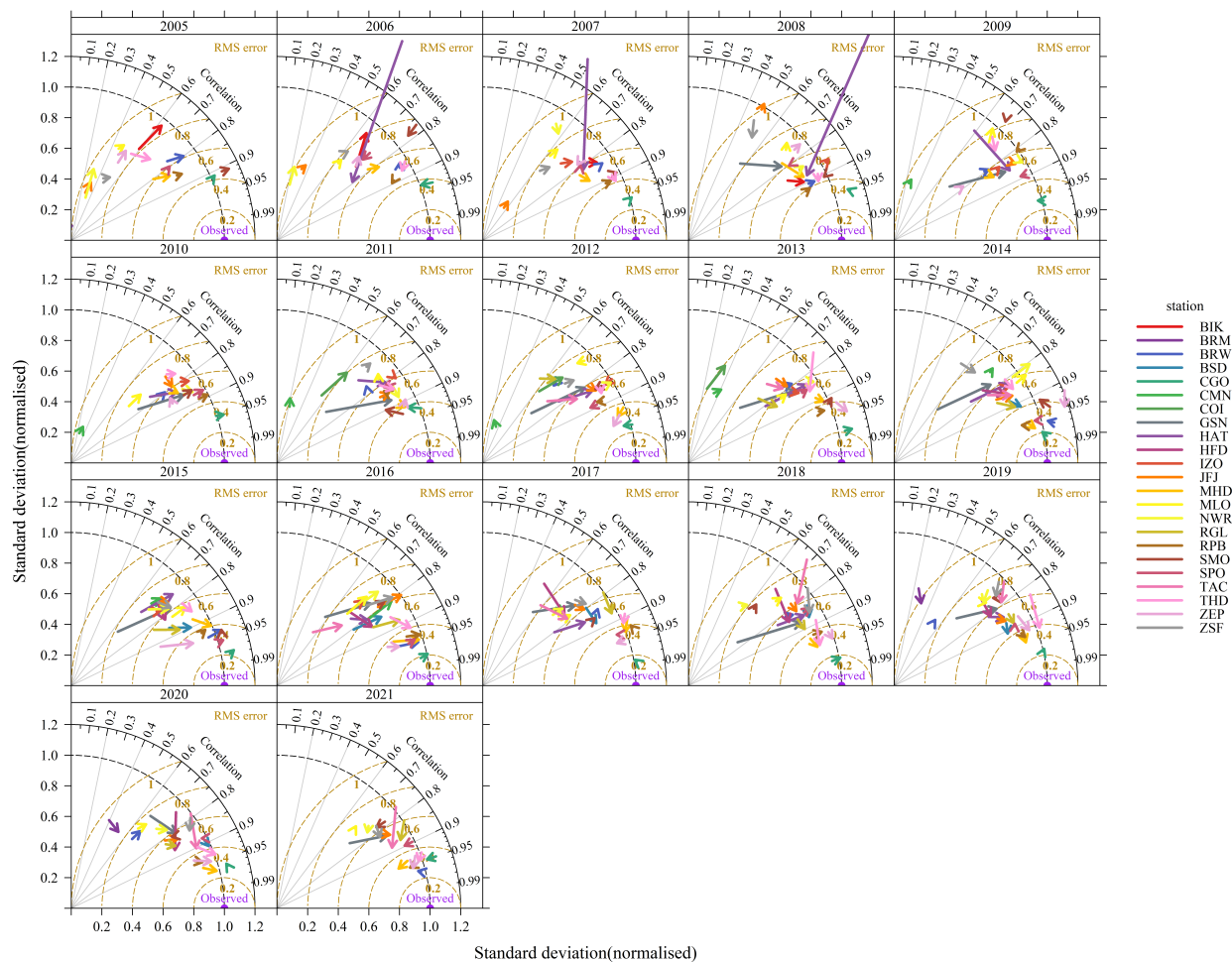
Figure S24. Taylor diagrams for comparing the *a priori* and *a posteriori* simulated mole fractions to the observed mixing ratios at all continuous stations, for the years 2005-2021. The diagram summarizes the match between observed and simulated values, by showing three statistics: (i) the Pearson correlation coefficient, represented by the azimuthal angle, (ii) the (against observations) normalized root mean square error (RMS) which is proportional to the distance from the as "observed" labeled purple dot, and (iii) the normalized standard deviation, represented by the radial distance from the origin. Each colored arrow represents a station, where the tail represents the *a priori* and the head the *a posteriori* simulated mole fractions. The length of each arrow, represents the difference between the *a priori* and *a posteriori* modeled mixing ratios with respect to the observed mixing ratios, indicating the correction made by the inversion. We observe large reductions in root mean square error for HAT and GSN almost across all the years. BRM, HFD, TAC, RGL, and ZSF also show significant improvements in error and correlation. The Taylor diagram can clearly distinguish the background stations from the stations that regularly capture emission events. However, also for background stations, small improvements can be seen.

S2 Supplementary Tables

Table S1. List of surface stations continuously monitoring SF_6.

Site ID	Station	Organisation	Latitude	Longitude	Altitude[a]	Period	total number
BIK	Bialystok, Poland	MPI	53.2°N	23.0°E	180	2005-2008	9412
BRM	Beromünster, Switzerland	EMPA	47.2°N	8.2°E	797	2019-2020	8066
BRW	Barrow, Alaska, USA	NOAA/GML/CATS	71.3°N	156.6°W	18	2005-2021	184428
BSD	Bilsdale, UK	UNIVBRIS	54.4°N	1.1°W	379	2014-2020	464423
CGO	Cape Grim, Tasmania	CSIRO/AGAGE	40.7°S	144.7°E	164	2005-2021	70652
CMN*	Monte Cimone, Italy	UNIURB/AGAGE	44.2°N	10.7°E	2172	2009-2017	126546
COI	Cape Ochiishi, Japan	NIES	43.2°N	145.5°E	100	2011-2013	33412
GSN	South Korea	KNU/AGAGE	33.3°N	126.2°E	89	2008-2021	33785
HAT	Hateruma, Japan	NIES	24.1°N	123.8°E	47	2005-2019	104922
HFD	Heathfield, UK	UNIURB	51.0°N	0.2°E	157	2014-2020	408800
IZO*	Izaña, Tenerife	AEMET	28.3°N	16.5°W	2403	2007-2016	92557
JFJ*	Jungfraujoch, Switzerland	EMPA/AGAGE	46.5°N	8.0°E	3584	2005-2021	87450
MHD	Mace Head, Ireland	UNIVBRIS/AGAGE	53.3°N	9.9°W	26	2005-2021	66944
MLO*	Mauna Loa, Hawaii, USA	NOAA/GML/CATS	19.5°N	155.6°W	3407	2005-2021	179396
NWR*	Niwot Ridge, Colorado, USA	NOAA/GML/CATS	40.0°N	105.5°W	3028	2005-2021	133475
RGL	Ridge Hill, UK	UNIVBRIS	52.0°N	2.5°W	294	2012-2021	501617
RPB	Ragged Point, Barbados	UNIVBRIS/AGAGE	13.2°N	59.4°W	50	2005-2021	55463
SMO	Cape Matatulu, American Samoa, USA	NOAA/GML/CATS/AGAGE	14.3°S	170.6°W	87	2005-2021	121670
SPO	South Pole, Antarctica	NOAA/GML/CATS	90.0°S	24.8°W	2820	2005-2021	174672
SUM	Summit, Greenland	NOAA/GML/CATS	72.6°N	38.5°W	3228	2007-2017	98620
TAC	Tacolneston Tall Tower, UK	UNIVBRIS/AGAGE	52.5°N	1.1°E	183	2012-2021	57590
THD	Trinidad Head, USA	SIO/EAS/AGAGE	41.1°N	124.2°W	127	2005-2021	68466
ZEP	Zeppelin, Ny-Alesund, Norway	NILU/AGAGE	78.9°N	11.9°E	490	2005-2021	42102
ZSF*	Zugspitze-Schneefernerhaus, Germany	UBAG	47.4°N	11.0°E	2670	2005-2021	156336

[a] The altitude specifies the sampling height in meters above sea level. Stations considered as mountain sites are marked with an asterisk.

Table S2. List of flask measurement sampling sites (1)

Site ID	Station	Organisation	Latitude	Longitude	Altitude^a	Period	total number
ABP	Arembepe, Bahia, Brazil	NOAA/GML/CCGG/INPE	12.8°S	38.2°W	6	2006-2010	114
ALT	Alert, Canada	NOAA/GML/CCGG	82.5°N	62.5°W	190	2005-2021	1162
ALT	Alert, Canada	NOAA/HATS	82.5°N	62.5°W	200	2005-2013	425
AMT	Argyle, Maine, USA	NOAA/GML/CCGG	45.0°N	68.7°W	157	2005-2008	72
AMT	Argyle, Maine, USA	NOAA/HATS	45.0°N	68.7°W	160	2008-2021	1781
AMY	Anmyeon-do, Republic of Korea	NOAA/GML/CCGG	36.5°N	126°E	87.0	2013-2021	340
ASC	Ascension Island, UK	NOAA/GML/CCGG	8.0°S	14.4°W	90	2005-2021	1468
ASK	Assekrem, Algeria, UK	NOAA/GML/CCGG	23.3°N	5.6°E	2715	2005-2020	713
AZR	Serreta (Terceira), Portugal	NOAA/GML/CCGG	38.8°N	27.4°W	24	2005-2021	489
BAL	Baltic Sea, Poland	NOAA/GML/CCGG	55.4°N	17.2°E	28	2005-2011	545
BAO	Boulder Atmospheric Observatory, Colorado, USA	NOAA/GML/GGGRN	40.1°N	105.0°W	1884	2007-2016	2688
BHD	Baring Head, New Zealand	NOAA/GML/CCGG	41.4°S	174.9°E	912	2005-2021	266
BKT	Bukit Kototabang, Indonesia	NOAA/GML/CCGG	0.2°S	100.3°E	875	2005-2021	728
BME	St. Davids Head, Bermuda	NOAA/GML/CCGG	32.4°N	64.6°W	17	2005-2010	77
BMW	Tudor Hill (Bermuda), UK	NOAA/GML/CCGG	32.3°N	64.9°W	55	2005-2021	655
BRW	Barrow, Alaska, USA	NOAA/GML/CCGG	71°N	156.6°W	16/28	2005 - 2021	1656
BRW	Barrow, Alaska, USA	NOAA/HATS	71°N	156.6°W	27	2005 - 2013	400
BSC	Constanta (Black Sea), Romania	NOAA/GML/CCGG	44.2°N	28.7°E	5	2005-2011	330
CBA	Cold Bay (AK), USA	NOAA/GML/CCGG	55.2°N	162.7°W	49	2005-2021	1437
CGO	Cape Grim, Tasmania	NOAA/GML/CCGG	40.7°S	144.7°E	164	2005-2021	623
CGO	Cape Grim, Tasmania	NOAA/HATS	40.7°S	144.7°E	164	2005-2013	344
CHR	Christmas Island, Kiribati	NOAA/GML/CCGG	1.7°N	157.2°W	5	2005-2020	463
CIB	Centro de Investigacion de la Baja Atmosfera (CIBA), Spain	NOAA/GML/CCGG	41.8°N	4.9°W	850	2009-2021	547
CPT	Cape Point, South Africa	NOAA/GML/CCGG	34.4°S	18.5°E	260	2010-2021	398
CRV	Carbon in Arctic Reservoirs Vulnerability Experiment (CARVE), US	NOAA/HATS	65.0°N	147.6°W	643	2012-2017	79
CRV	Carbon in Arctic Reservoirs Vulnerability Experiment (CARVE), US	NOAA/GML/GGGRN	65.0°N	147.6°W	643	2011-2021	1535
CRZ	Crozet Island, France	NOAA/GML/CCGG	46.4°S	51.8°E	202	2005-2021	733
DSI	Dongsha Island, Taiwan	NOAA/GML/CCGG	20.7°N	116.7°E	8	2010-2021	473
EIC	Easter Island, Chile	NOAA/GML/CCGG	27.2°S	109.4°W	64	2005-2019	550
GMI	Guam (Mariana Island), USA	NOAA/GML/CCGG	13.4°N	144.7°E	7	2005-2021	923
HBA	Halley, UK	NOAA/GML/CCGG	75.6°S	26.2°W	35	2005-2021	572
HFM	Harvard Forest (MA), USA	NOAA/GML/GGGRN	42.5°N	72.2°W	370	2016	12
HPB	Hohenpeissenberg, Germany	NOAA/GML/CCGG	47.8°N	11.0°E	941	2006-2021	841
HSU	Humboldt State University, USA	NOAA/GML/CCGG	41.1°N	124.6°W	8	2008-2017	87
HUN	Hegyhatsal, Hungary	NOAA/GML/CCGG	47.0°N	16.6°E	344	2005-2021	741
ICE	Storhofdi, Iceland	NOAA/GML/CCGG	63.4°N	20.3°W	126	2005-2021	846
IZO	Izaña, Tenerife	NOAA/GML/CCGG	28.3°N	16.5°W	2378	2005 - 2021	804
KEY	Key Biscane (FL), USA	NOAA/GML/CCGG	25.7°N	80.2°W	6	2005-2021	692
KLM	Kohler Mesa, USA	NOAA/GML/GGGRN	40.0°N	105.3°W	1730	2006	47
KUM	Cape Kumukahi (HI), USA	NOAA/GML/CCGG	19.5°N	154.8°W	5	2005-2021	1676
KUM	Cape Kumukahi (HI), USA	NOAA/HATS	19.7°N	155.0°W	36	2005-2013	434
KZD	Sary Taukum, Kazakhstan	NOAA/GML/CCGG	44.1°N	76.9°E	600	2005-2009	224
KZM	Plateau Assy, Kazakhstan	NOAA/GML/CCGG	43.2°N	77.9°E	2524	2005-2009	214
LEF	Park Falls (WI), USA	NOAA/GML/CCGG	45.9°N	90.3°W	868	2005-2021	142
LEF	Park Falls (WI), USA	NOAA/GML/GGGRN	45.9°N	90.3°W	868	2006-2021	3414
LEF	Park Falls (WI), USA	NOAA/HATS	45.9°N	90.3°W	482	2005-2013	362
LEW	Lewisburg, Pennsylvania, USA	NOAA/GML/GGGRN	40.9°N	76.9°W	261	2015-2021	717
LLB	Lac La Biche, Alberta, Canada	NOAA/GML/CCGG	55.0°N	112.5°W	568	2008-2013	213
LLN	Lulin, Taiwan, Province of China	NOAA/GML/CCGG	23.5°N	120.9°E	2867	2006-2021	604
LMP	Lampedusa, Italy	NOAA/GML/CCGG	35.5°N	12.6°E	50	2006-2021	659

^{a} The altitude specifies the sampling height in meters above sea level.

Table S3. List of flask measurement sampling sites (2).

Site ID	Station	Organisation	Latitude	Longitude	Altitude[a]	Period	total number
MBO	Mt. Bachelor Observatory, USA	NOAA/GML/GGGRN	44.0° N	121.7° W	2742	2011-2021	1914
MEX	Mex High Altitude Global Climate Observation Center, Mexico	NOAA/GML/CCGG	19.0° N	97.3° W	4469	2009-2021	488
MHD	Mace Head, Ireland	NOAA/GML/CCGG	53.3° N	9.9° W	26	2005-2021	777
MHD	Mace Head, Ireland	NOAA/HATS	53.3° N	9.9° W	42	2005-2013	193
MID	Sand Island, Midway, USA	NOAA/GML/CCGG	28.2° N	177.4° W	12	2005-2021	841
MKN	Mt. Kenya, Kenya	NOAA/GML/CCGG	0.1° S	37.3° E	3649	2005-2011	126
MLO	Mauna Loa, Hawaii, USA	NOAA/GML/CCGG	19.5° N	155.6° W	3437	2005-2021	1746
MLO	Mauna Loa, Hawaii, USA	NOAA/HATS	19.5° N	155.6° W	3433	2005-2013	432
MLO	Mauna Loa, Hawaii, USA	NOAA/GML/GGGRN	19.5° N	155.6° W	3433	2021	68
MRC	Marcellus Pennsylvania, USA	NOAA/GML/GGGRN	41.5° N	76.3° W	652	2015-2021	713
MSH	Mashpee, Massachusetts, USA	NOAA/GML/GGGRN	41.7° N	70.5° W	78	2016-2021	503
MVY	Marthas Vineyard, Massachusetts, USA	NOAA/GML/GGGRN	41.3° N	70.6° W	16	2007-2011	210
MWO	Mt. Wilson Observatory, USA	NOAA/GML/GGGRN	34.2° N	118.1° W	1775	2010-2021	4437
NAT	Natal, Brazil	NOAA/GML/CCGG/INPE	5.6° S	35.2° W	49	2010-2020	385
NMB	Gobabeb, Namibia	NOAA/GML/CCGG	23.6° S	15.0° E	461	2006-2021	614
NWB	NW Baltimore, USA	NOAA/GML/CCGG	39.3° N	76.7° W	190	2018-2021	41
NWR	Niwot Ridge, Colorado	NOAA/GML/CCGG	40.1° N	-105.6° W	3526	2005 - 2021	847
NWR	Niwot Ridge, Colorado	NOAA/HATS	40.1° N	-105.6° W	3523	2005 - 2013	342
NWR	Niwot Ridge, Colorado	NOAA/GML/GGGRN	40.1° N	-105.6° W	3523	2005 - 2021	3712
OBN	Obninsk, Colorado, Russia	NOAA/HATS	55.1° N	36.6° E	484	2005-2009	146
OXK	Ochsenkopf, Germany	NOAA/GML/CCGG	50.0° N	11.8° E	1181	2006-2021	404
PAL	Pallas, Finland	NOAA/GML/CCGG	68.0° N	24.1° E	570	2005-2021	797
PCO	Pico, Azores, Portugal	NOAA/HATS	38.5° N	28.4° W	2230	2010-2011	6
PSA	Palmer Station, USA	NOAA/GML/CCGG	64.9° S	64.0° W	15	2005-2021	835
PSA	Palmer Station, USA	NOAA/HATS	64.9° S	64.0° W	13	2005-2013	183
PTA	Point Arena (CA), USA	NOAA/GML/CCGG	39.0° N	123.7° W	22	2005-2011	291
RPB	Ragged Point, Barbados	NOAA/GML/CCGG	13.2° N	59.4° W	20	2005-2021	841
SCT	Beech Island, South Carolina, USA	NOAA/GML/GGGRN	33.4° N	81.8° W	420	2008-2021	2778
SDZ	Shangdianzi, Peoples Republic of China	NOAA/GML/CCGG	40.6° N	117.1° E	298	2009-2015	154
SEY	Mahe Island, Seychelles	NOAA/GML/CCGG	4.7° S	55.5° E	7	2005-2021	773
SGP	Southern Great Plains, Oklahoma, USA	NOAA/GML/CCGG	36.7° N	97.5° W	374	2005-2021	831
SGP	Southern Great Plains, Oklahoma, USA	NOAA/GML/GGGRN	36.7° N	97.5° W	374	2010-2021	298
SHM	Shemya Island, USA	NOAA/GML/CCGG	52.7° N	174.1° E	28	2005-2021	797
SMO	Cape Matatulu, American Samoa, USA	NOAA/GML/CCGG	14.3° S	170.6° W	60	2005-2021	1561
SMO	Cape Matatulu, American Samoa, USA	NOAA/HATS	14.3° S	170.6° W	77	2005-2013	451
SPO	South Pole, Antarctica	NOAA/GML/CCGG	90.0° S	24.8° W	2820	2005-2021	1228
SPO	South Pole, Antarctica	NOAA/HATS	90.0° S	24.8° W	2837	2005-2021	296
STM	Ocean Station M, Norway	NOAA/GML/CCGG	66.0° N	2.0° E	5	2005-2009	467
STR	Sutro Tower, San Francisco, California, USA	NOAA/GML/GGGRN	37.8° N	122.5° W	426	2007-2021	6790
SUM	Summit, Greenland	NOAA/GML/CCGG	72.6° N	38.5° W	3214	2005-2021	873
SUM	Summit, Greenland	NOAA/HATS	72.6° N	38.5° W	3212	2005-2013	233
SYO	Syowa Station, Antarctic, Japan	NOAA/GML/CCGG	69.0° S	39.6° E	17	2005-2021	403
TAC	Tacolneston Tall Tower, UK	NOAA/GML/CCGG	52.5° N	1.1° E	236	2014-2016	50
TAP	Tae-ahn Peninsula, Republic of Korea	NOAA/GML/CCGG	36.7° N	126.1° E	21	2005-2021	835
THD	Trinidad Head, USA	NOAA/GML/CCGG	41.1° N	124.2° W	112	2005-2017	615
THD	Trinidad Head, USA	NOAA/HATS	41.1° N	124.2° W	120	2005-2013	382
TIK	Tiksi, Russian Federation	NOAA/GML/CCGG	71.6° N	128.9° E	29	2011-2018	340
TPI	Taiping Island	NOAA/GML/CCGG	10.4° N	144.4° E	9	2019 - 2021	121
USH	Ushuaia, Argentina	NOAA/GML/CCGG	54.8° S	68.3° W	32	2005-2021	616
USH	Ushuaia, Argentina	NOAA/HATS	54.8° S	68.3° W	15	2005-2010	46
UTA	Wendover (UT), USA	NOAA/GML/CCGG	39.9° N	113.7° W	1332	2005-2021	910
UUM	Ulaan Uul, Mongolia	NOAA/GML/CCGG	44.5° N	111.1° E	1012	2005-2021	734
WBI	West Branch, Iowa, USA	NOAA/GML/GGGRN	41.7° N	91.4° W	621	2007-2021	3657
WGC	Walnut Grove, California, USA	NOAA/GML/GGGRN	38.3° N	121.5° W	94	2007-2021	2590
WIS	Sede Boker, Israel	NOAA/GML/CCGG	30.6° N	34.9° E	379	2005-2021	815
WKT	Moody, Texas, USA	NOAA/GML/CCGG	31.3° N	97.3° W	372	2005-2010	176
WKT	Moody, Texas, USA	NOAA/GML/GGGRN	31.3° N	97.3° W	372	2006-2021	3101
WLG	Mt. Waliguan, Peoples Republic of China	NOAA/GML/CCGG	36.3° N	100.9° E	3827	2005-2021	660
ZEP	Zeppelin, Ny-Alesund, Norway	NOAA/GML/CCGG	78.9° N	11.9° E	479	2005-2021	848

[a] The altitude specifies the sampling height in meters above sea level.

Table S4. Measurements from moving platforms.

Site ID	Measurements Site	Organisation	Altitude$^{\alpha}$ range	Period	total number	platform
AAO	Airborne Aerosol Observatory, Bondville, Illinois, USA	NOAA/GML/CCAVPN	373 - 4859	2006 - 2009	3001	aircraft
ACG	Alaska Coast Guard, USA	NOAA/GML/CCAVPN	48 - 8857	2009 - 2021	1758	aircraft
ACT	Atmospheric Carbon and Transport - America, USA	NOAA/GML/CCAVPN	117 - 9060	2016 - 2019	1477	aircraft
AOC	Atlantic Ocean Cruise	NOAA/ESRL/GMD	10	2005	16	ship
BAO	Boulder Atmospheric Observatory, Colorado, USA	NOAA/GML/CCAVPN	1849 - 4794	2008	12	aircraft
BGI	Bradgate, Iowa, USA	NOAA/GML/CCAVPN	598 - 8074	2005	296	aircraft
BII	Biak, Indonesia	MUE/TU/NIPR	17200 - 28700	2015	7	balloon
BNE	Beaver Crossing, Nebraska, USA	NOAA/GML/CCAVPN	597 - 8157	2005 - 2011	969	aircraft
CAR	Briggsdale, Colorado,USA	NOAA/GML/CCAVPN	1585 - 8469	2005 - 2021	4025	aircraft
CARIBIC	Civil Aircraft for the Regular Investigation of the atmosphere Based on an Instrument Container	KIT/MPIC	947 - 12525	2005 - 2020	7379	aircraft
CMA	Offshore Cape May, New Jersey, USA	NOAA/GML/CCAVPN	247 - 8119	2005 - 2021	3073	aircraft
CON	CONTRAIL (Comprehensive Observation Network for TRace gases by AIrLiner)	NIES/MRI	780 - 13110	2005 - 2017	3192	aircraft
CRS	Miscellaneous Cruises	NOAA/ESRL/GMD	20	2005 - 2011	120	ship
CRV	Carbon in Arctic Reservoirs Vulnerability Experiment (CARVE), USA	NOAA/GML/CCAVPN	2 - 5526	2011 - 2017	2446	aircraft
DND	Dahlen, North Dakota, USA	NOAA/GML/CCAVPN	517 - 8131	2005 - 2016	1941	aircraft
DRP	Drake Passage	NOAA/ESRL/GMD	10	2005 - 2017	375	ship
ECO	East Coast Outflow, USA	NOAA/GML/CCAVPN	146 - 4564	2018, 2020	343	aircraft
ESP	Estevan Point, British Columbia, Canada	NOAA/GML/CCAVPN	18 - 5819	2005 - 2021	4310	aircraft
ETL	East Trout Lake, Saskatchewan, Canada	NOAA/GML/CCAVPN	599 - 7823	2005 - 2020	3041	aircraft
FAM	FAAM Aircraft, United Kingdom	NOAA/ESRL/GMD	129 - 2000	2014 - 2015	12	aircraft
FWI	Fairchild, Wisconsin, USA	NOAA/GML/CCAVPN	589 - 8071	2005	314	aircraft
HAA	Molokai Island, Hawaii, USA	NOAA/GML/CCAVPN	315 - 8096	2005 - 2008	976	aircraft
HFM	Harvard Forest, Massachusetts, USA	NOAA/GML/CCAVPN	582 - 8062	2005 - 2007	717	aircraft
HIL	Homer, Illinois USA	NOAA/GML/CCAVPN	21 - 8117	2005 - 2021	3097	aircraft
INX	INFLUX (Indianapolis Flux Experiment), USA	NOAA/GML/CCAVPN	302 - 3518	2010 - 1016	350	aircraft
LEF	Park Falls, Wisconsin, USA	NOAA/GML/CCAVPN	558 - 4034	2005 - 2017	3268	aircraft
MCI	Mid Continent Intensive, USA	NOAA/GML/CCAVPN	359 - 3702	2007 - 2008	128	aircraft
MRC	Marcellus Pennsylvania, USA	NOAA/GML/CCAVPN	879 - 3123	2015	77	aircraft
NHA	Offshore Portsmouth, New Hampshire (Isles of Shoals) USA	NOAA/GML/CCAVPN	115 - 8136	2005 - 2021	3689	aircraft
NSA	North Slope, Alaska, NSA	NOAA/GML/CCAVPN	10 - 6377	2015 - 2016	378	aircraft
NSK	Northern Saskatchewan, Canada	NOAA/GML/CCAVPN	819 - 6576	2020 - 2021	45	aircraft
OIL	Oglesby, Illinois	NOAA/GML/CCAVPN	529 - 8121	2005	338	aircraft
PAN	Pantanal, Mato Grosso do Sul, Brazil	INPE	152 - 4419	2017 - 2019	438	aircraft
PAO	Pacific-Atlantic Ocean	NOAA/ESRL/GMD	10	2006	90	ship
PFA	Poker Flat, Alaska, USA	NOAA/GML/CCAVPN	131 - 7604	2005 - 2021	3759	aircraft
POC	Pacific Ocean	NOAA/ESRL/GMD	20	2005 - 2017	1834	ship
RTA	Rarotonga, Cook Islands	NOAA/GML/CCAVPN	15 - 6527	2005 - 2021	1943	aircraft
SAN	Santarem, Brazil	INPE	152 - 4268	2007 - 2009	927	aircraft
SCA	Offshore Charleston, South Carolina, USA	NOAA/GML/CCAVPN	218 - 13278	2005 - 2021	3404	aircraft
SGP	Southern Great Plains, Oklahoma, USA	NOAA/GML/CCAVPN	172 - 12926	2006 - 2021	6587	aircraft
SYO	Syowa Station, Antarctica, Japan	TU/AND/MUE	14600 - 28500	2008, 2012, 2013	6	balloon
TGC	Offshore Corpus Christi, Texas, USA	NOAA/GML/CCAVPN	243 - 8207	2005 - 2021	2589	aircraft
THD	Trinidad Head, California, USA	NOAA/GML/CCAVPN	152 - 8131	2005 - 2021	2437	aircraft
ULB	Ulaanbaatar, Mongolia	NOAA/GML/CCAVPN	1511 - 4425	2004 - 2019	503	aircraft
WBI	West Branch, Iowa, USA	NOAA/GML/CCAVPN	543 - 8204	2005 - 2021	2847	aircraft
WGC	Walnut Grove, California, USA	NOAA/GML/CCAVPN	6 - 3177	2008 - 2009	159	aircraft
WPC	Western Pacific, USA	NOAA/ESRL/GMD/NIWA	8 - 10	2005 - 2013	242	ship
	NOAA/ESRL/GMD/HATS Trace Gas Measurements from Airborne Platforms, including the NASA campaigns AV-DEMO , AVE-05, CR-AVE, TC4 START-08, HIPPO, GLOPAC, ATTREX, ATOM, POSIDON					

$^{\alpha}$ The altitude specifies the sampling height in meters above sea level.

Table S5. Organizations and international observation networks and programs that provided measurement data, and their respective acronyms

Abbrevation	Organization / Program
AEMET	Agencia Estatal de Meteorología (State Meteorological Agency, Spain)
AGAGE	Advanced Global Atmospheric Gases Experiment
CSIRO	Commonwealth Scientific and Industrial Research Organisation (Australia)
EAS	School of Earth and Atmospheric Sciences, Georgia Institute of Technology (USA)
EMPA	Eidgenössische Materialprüfungs- und Forschungsanstalt (Swiss Federal Laboratories for Materials Science and Technology)
INPE	Instituto Nacional de Pesquisas Espaciais (Brazil)
KIT	Karlsruhe Institute of Technology (Germany)
KNU	Kyungpook National University (South Korea)
MPI	Max Planck Institute (Germany)
MPIC	Max Planck Institute for Chemistry (Germany)
MRI	Meteorological Research Institute (Japan)
MUE	Miyagi University of Education (Japan)
NIES	National Institute for Environmental Studies (Japan)
NILU	Norwegian Institute for Air Research
NIPR	National Institute of Polar Research (Japan)
NIWA	National Institute of Water and Atmospheric Research, New Zealand
NOAA	National Oceanic and Atmospheric Administration (USA)
CATS	Chromatograph for Atmospheric Trace Species
CCAVPN	Carbon Cycle Aircraft Vertical Profile Network
CCGG	Carbon Cycle Greenhouse Gases group
ESRL	Earth System Research Laboratory
GGGRN	Global Greenhouse Gas Reference Network
GMD	Global Monitoring Division
GML	Global Monitoring Laboratory
HATS	Halocarbons and other Atmospheric Trace Species
SIO	Scripps Institution of Oceanography (USA)
TU	Tohoku University - Center for Atmospheric and Oceanic Studies
UBAG	Umweltbundesamt (German Federal Environmental Agency)
UNIURB	Università degli Studi di Urbino "Carlo Bo" (University of Urbino, Italy)
UNIVBRIS	University of Bristol (UK)

Table S6. Nudging kernel configuration used to run FLEXPART CTM

Nudging kernel configurations			
kernel dimensions	surface stations	ship measurements	aircraft measurements
latitudinal kernel width h_y [°]	$[1\text{-}25]^a$	10	$1 + 15 \cdot arctan\left(\frac{altitude^b}{1000m}\right)$
longitudinal kernel width h_x [°]	same as h_y	same as h_y	same as h_y
kernel height h_z [m]	500 for $h_y > 5°$ 300 for $h_y \leq 5°$	300	$20 \cdot \frac{h_y}{1°}$
temporal kernel length h_t [s]	$86400 \cdot \frac{h_y}{1°}$	$86400 \cdot \frac{h_y}{1°}$	$86400 \cdot \frac{h_y}{1°}$
kernel relaxation time τ [s]	1800	1800	1800

^{a} h_y depends on the standard deviation of measurements in a 3-day time interval for continuous measurements ($h_y = 5° \cdot \frac{0.08ppt}{std}$) and
a 60-day time interval for flask measurements ($h_y = 5° \cdot \frac{0.15ppt}{std}$) .

^{b} Altitude indicates the measurement altitude in meters above ground level.

Table S7. Statistical values comparing detrended modeled with detrended observed mole fractions at individual measurement stations, using EP7 as *a priori* emissions. The detrending was done, as for all stations the trend is so strong that very high correlation values of almost 100% would be obtained otherwise.

measurement site	a priori r^2 [%]	a posteriori r^2 [%]	a priori MSE [1000 ppt^2]	a posteriori MSE [1000 ppt^2]
bik	56	60	6.30	6.19
brm	28	37	49.2	45.0
brw	81	81	5.27	4.96
bsd	53	69	6.57	4.18
cgo	91	91	1.05	1.04
cmn	40	44	43.7	37.8
coi	41	53	20.9	18.2
gsn	65	81	405	198
hat	65	83	115	51
hfd	60	79	21.00	9.58
izo	50	51	4.72	4.63
jfj	59	62	20.2	18.3
mhd	92	94	2.72	2.11
mlo	69	69	11.5	10.3
nwr	84	85	10.02	8.42
rgl	56	72	7.51	5.33
rpb	96	96	2.07	2.03
smo	93	93	3.70	3.65
spo	77	77	3.06	3.06
sum	43	45	5.25	5.02
tac	76	85	17.8	11.0
thd	62	68	3.87	2.60
zep	97	98	2.27	1.64
zsf	91	93	13.1	10.6

S3 Measurement data sets

Observations from continuous surface stations

5 Table S1 lists all the surface stations continuously monitoring SF_6. Measurements at CGO, JFJ, MHD, RPB, SMO, TAC, THD, and ZEP were provided by the international observation network AGAGE (Prinn et al., 2018). Data from BRW, MLO, NWR, SMO, SPO, and SUM were provided by the NOAA/GML Chromatograph for Atmospheric Trace Species (CATS) program (Dutton and Hall, 2023). Data from CMN (Maione et al., 2013), COI (Tohjima et al., 2002), IZO (Gomez-Pelaez and Ramos, 2009), RGL (Stavert et al., 2019), and ZSF (Zellweger et al., 2020) were found in the WDCGG data base https:

10 //gaw.kishou.go.jp/search (di Sarra et al., 2022). Observations from HFD (Arnold et al., 2019), BSD (O'Doherty et al., 2019) were found at the CEDA data base (CEDA, 2023), and measurements for ZEP (2005-2010) were found at the EBAS database (Tørseth et al., 2012). For the observations at BIK (Popa et al., 2010), BRM (Rust et al., 2022), GSN (Kim et al., 2012), and HAT (Saikawa et al., 2012) we refer to E. Popa <epopa2@yahoo.com>, S. Reinmann <stefan.reimann@empa.ch>, S. Park <sparky@knu.ac.kr>, and T. Saito <saito.takuya@nies.go.jp>, respectivley

Surface flask measurements

Table S2 and S3 list all the surface flask measurement sampling sides. Measurements at ABP, ALT, AMT, AMY, ASC, ASK, AZR, BAL, BHD, BKT, BME, BMW, BRW, BSC, CBA, CGO, CHR, CIB, CPT, CRZ, DSI, EIC, GMI, HBA, HPB, HSU, HUN, ICE, IZO, KEY, KUM, KZD, KZM, LEF, LLB, LLN, LMP, MEX, MHD, MID, MKN, MLO, NAT, NMB, NWR, OXK, PAL, PSA, PTA, SDZ, SEY, SGP, SHM, SMO, SPO, STM, SUM, SYO, TAP, THD, TIK, TPI, USH, UTA, UUM, WIS, WKT,

20 WLG, ZEP were provided by the Atmospheric SF_6 Dry Air Mole Fractions from the NOAA GML Carbon Cycle Cooperative Global Air Sampling Network (Lan et al., 2023; Dlugokencky et al., 2020). For APB and NAT, INPE collected the samples, and the analysis was done together with NOAA/GML. NOAA Global Greenhouse Gas Reference Network provided flask-air PFP sample measurements of SF_6 at Tall Towers and other Continental Sites (Andrews et al., 2022) at BAO, CRV, HFM, KLM, LEF, LEW, MBO, MLO, MRC, MSH, MVY, MWO, NWB, NWR, SCT, SGP, STR, WBI, WGC, WKT. Measurements at ALT,

25 AMT, CGO, CRV, KUM, LEF, MHD, MLO, NWR, OBN, PCO, PSA, SPO, SUM, THD, USH were provided by NOAA ESRL Halocarbons and other Atmospheric Trace Species (HATS) (Elkins and Dutton, 2008; Hall et al., 2011) and were part of the NOAA ObsPACK SF_6 data set (NOAA Carbon Cycle Group ObsPack Team, 2018).

Measurements from moving platforms

Table S4 lists the measurements from moving platforms. AAO, ACG, ACT, BAO, BGI, BNE, CAR, CMA, CRV, DND, DRP, 30 ECO, ESP, ETL, FWI, HAA, HFM, HIL, INX, LEF, MCI, MRC, NHA, NSA, NSK, OIL, PFA, RTA, SCA, SGP, TGC, THD, ULB, WBI, WGC were provided by the Atmospheric Sulfur Hexafluoride Dry Air Mole Fractions from the NOAA GML Carbon Cycle Aircraft Vertical Profile Network (McKain et al., 2022). Observations at AOC, BII, CON, CRS, DRP, FAM, PAO, POC, SYO, WPC are part of NOAA ObsPACK SF_6 data set (NOAA Carbon Cycle Group ObsPack Team, 2018).

Observations at SAN and PAN were provided by INPE (D'Amelio et al., 2024). IAGOS-CARIBIC Aircraft measurements were provided by Schuck and Obersteiner (2024). NOAA/ESRL/GMD/HATS Trace Gas Measurements from Airborne Platforms (Elkins et al., 2020) provide observations from NASA aircraft measurement campaigns including UAV-DEMO (ALTAIR) (Fahey et al., 2006), AVE-05 (WB57) (Petropavlovskikh et al., 2008), CR-AVE (WB57) (Gensch et al., 2008), TC4 (WB57) (Salawitch et al., 2008), START-08 (GV) (Schauffler et al., 2010), HIPPO (GV) (Wofsy, 2011), GLOPAC (GHAWK) (Newman et al., 2010), ATTREX (GHAWK) (Jensen et al., 2013), ATOM (DC8) (Wofsy et al., 2018), POSIDON (WB57) (Jensen et al., 2020).

S4 Standardization of observations

The measurements from different providers were calibrated with four calibration scales: NIES-2008, WMO-SF$_6$-X2006, WMO-SF$_6$-X2014 and SIO-2005. We standardized all observations to the SIO-2005 calibration scale. To convert from WMO-SF$_6$-X2014 to SIO-2005 scale, we used the factor of 1.002 presented in Guillevic et al. (2018). Note, however, that while according to Krummel et al. (2017), this factor seems appropriate for observations after 2010, it might be too low for earlier data and a factor of 1.008 would have been more appropriate. As the difference is, however, smaller than 1% we expect the impact on our inversion results to be negligible. For future applications, we recommend getting in contact with Paul Krummel <paul.krummel@csiro.au>. To convert the mole fractions from WMO-SF$_6$-X2006 to WMO-SF$_6$-X2014, we used the equation $y = ax2 + bx + c$, where y represents the SF$_6$ mole fractions on the X2014 scale, x represents the mole fractions on the X2006 scale, and the coefficients a, b, and c have values of $2.6821 \cdot 10^{-3}$, $9.7748 \cdot 10^{-1}$, and $3.5831 \cdot 10^{-2}$ (NOAA ESRL, 2014), respectively. The NIES-2008 calibrated data were divided by a factor of 1.013 (Saito, 2021).

S5 The initialization of FLEXPART CTM

SF$_6$ emissions are higher in the Northern than in the Southern Hemisphere, resulting in a substantial latitudinal gradient of SF$_6$ mole fractions. To address this in the initialization of the FLEXPART CTM, we provide a latitudinal SF$_6$ profile determined by interpolation of surface measurements in the first two weeks of the initialization. FLEXPART CTM disperses particles globally in proportion to air density, and according to the provided latitudinal profile. The SF$_6$ concentration in the stratosphere is influenced by the age of stratospheric air (AoA), defined as the average transport time of an air parcel from its entry into the stratosphere to any point within it (Waugh and Hall, 2002; Loeffel et al., 2022). Regions with high AoA have lower SF$_6$ concentrations, as they represent the lower tropospheric concentrations in the past, when the corresponding air left the troposphere. To address this, we use the MIPAS 3d AoA fields (Stiller et al., 2021) along with the average global concentrations calculated by Simmonds et al. (2020) to correct the initial concentration fields in the stratosphere. In detail, we calculate a 3d field of correction factors, by building the ratio between the SF$_6$ concentration at the initialization time and the concentration at the time given by the respective AoA value. Figure S25 shows the initial mole fraction field for 2005.
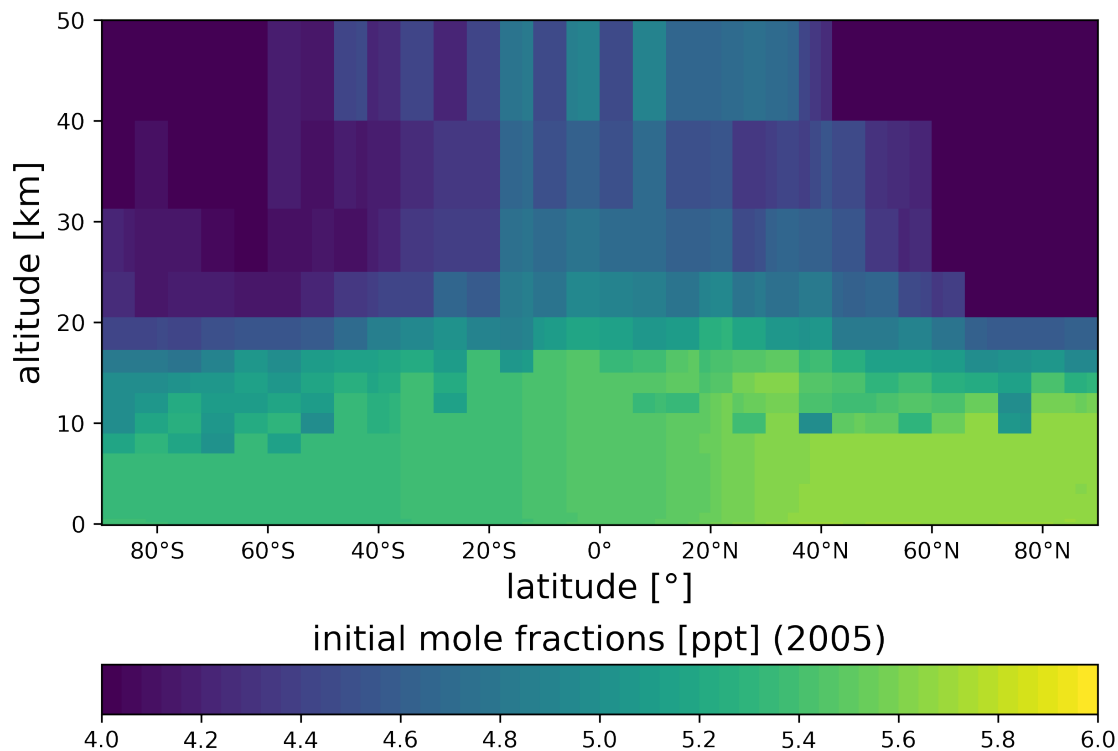
Figure S25. Initial field of SF$_6$ mole fractions used for the initialization in the year 2005.

S6 SF$_6$ emission in the GAINS model

SF$_6$ emissions originate from various sources such as mid- and high-voltage switches, magnesium production and casting, soundproof glazing, and a range of other applications including photovoltaic manufacturing, military applications, biomedical industry, fiber optic production, particle accelerators, and sports equipment. Within the GAINS model, four distinct sources of SF$_6$ emissions have been identified as follows:

High and mid voltage switches

SF$_6$ emissions primarily originate from the electrical equipment sector due to leakage, maintenance, and retirement (IPCC/TEAP, 2005). SF$_6$ functions as an electrical insulator in transmission and distribution equipment in electric systems, primarily within gas-insulated switch gears (GIS) employed in high and mid-voltage electric networks. Emission levels of SF$_6$ are affected by factors like the age of GIS, with older models exhibiting higher leakage rates than newer ones, and the size of the transmission network, as well as the recycling practices of obsolete equipment (Purohit and Höglund-Isaksson, 2017; Gambhir et al., 2017).

In this study, the GAINS model utilizes reported emissions for Annex-I countries from the years 2005, 2010, 2015, and 2020, as documented by UNFCCC (2023). For the historical years, SF$_6$ emissions in China are taken from Zhou et al. (2018) and Cui

et al. (2024). The GAINS model uses electricity generation as an activity variable for this sector. For other non-Annex-I (developing) countries, the emission factor for SF_6 per unit of electricity generated is taken from the average of Annex-I countries (UNFCCC, 2023) and applied in a consistent manner to all regions. In recent years, several alternatives to SF_6 in both mid- and
80   high-voltage electrical switch gear were developed. The GAINS model incorporated alternative substitutes for SF_6 in mid- and high-voltage electrical switch gear, including zero-GWP AIR, NOVEC-4710 with a GWP100 of 2100, and NOVEC-5110 with a GWP100 of 1 (Gschrey et al., 2022; Owens et al., 2021). Additionally, emissions can be reduced through recycling practices for used SF_6 switch gears, as mandated by F-gas Regulation (EC 842/2006) since 2010.

Magnesium production and casting

85   The casting and production of primary and secondary magnesium are recognized as significant sources of SF_6 atmospheric emissions. The gas is used as a shielding gas in magnesium foundries to protect the molten magnesium from reoxidizing whilst it is running to best casting ingots (IPCC, 2001). In this study, the GAINS model utilizes reported emissions for EU countries from the years 2005, 2010, 2015, and 2020 (UNFCCC, 2023). Activity data for non-EU countries on historic volumes of processed magnesium are taken from the United States Geological Survey (USGS, 2023) and the national communications to
90   UNFCCC (UNFCCC, 2023). The GAINS model uses value added for the manufacturing industry as an activity variable for this sector. An emission factor of 1 kg SF_6 per ton of processed metal is taken from Schwarz and Leisewitz (1999) and Tohka (2005). According to Fang et al. (2013), SF_6 consumption factor of 1.65 kg SF_6 per ton of magnesium is employed specifically for magnesium processing in China. While the 2006 EU F-gas regulation only restricted SF_6 usage in die-casting operations, the bans on SF_6 usage in recycling magnesium die-casting alloys were introduced in the 2014 EU F-gas regulation (DEFRA,
95   2014). In the GAINS model, SF_6 emissions from magnesium production and casting can be substituted by using sulfur dioxide or the recently introduced sustainable cover gas NOVEC-612, which has a GWP100 of 1.

Soundproof windows

Some European countries used significant amounts of SF_6 in soundproof windows. From 2006, EC 842/2006 bans the use of SF_6 in soundproof windows. Soundproof windows have a relatively long lifetime, and it is therefore expected that the stock of
100   SF_6 found in such windows in 2005 will be successively phased-out over a period of 25 years. The GAINS methodology to assess SF_6 emissions in soundproof windows is outlined in Purohit and Höglund-Isaksson (2017).

Other SF_6 sources

SF_6 has been used in several other applications including PV manufacturing, military applications, biomedical industry, fiber optic production, particle accelerators, and sports equipment. Activity data for these other sources of SF_6 emissions are taken
105   from emissions reported by countries to the (UNFCCC, 2023). Since 2006, EC 842/2006 has banned SF_6 in sports equipment and tires, with GAINS assuming full EU compliance.

Spatial distribution

The spatial distribution of SF_6 emissions in Europe (EU27, Iceland, Norway, Switzerland, United Kingdom of Great Britain and Northern Ireland) follows 4081 electrical substation locations, based on ENTSO-E data from Wiegmans (2016). In absence of more detailed information about substation characteristics, an equal distribution among substations in each country was chosen and individual locations aggregated at 0.1° resolution. For the remaining regions differentiated in the GAINS model, emissions are allocated using a gridded population proxy from the Gridded Population of the World (GPW) Doxsey-Whitfield et al. (2015) and Global Human Settlement Layer (GHSL) (EC-JRC, 2015). The gridded population data is processed at its highest initial resolution, spatially allocated to a region, and aggregated to the output resolution (0.1° in this case). The distribution of emissions is subsequently based on the relative population share within a region.

References

Andrews, A., Crotwell, A., Crotwell, M., Handley, P., Higgs, J., Kofler, J., Lan, X., Legard, T., Madronich, M., McKain, K., Miller, J., Moglia, E., Mund, J., Neff, D., Newberger, T., Petron, G., Turnbull, J., Vimont, I., Wolter, S., and NOAA Global Monitoring Laboratory: NOAA Global Greenhouse Gas Reference Network Flask-Air PFP Sample Measurements of SF6 at Tall Tower and other Continental Sites, 2005-Present [Data set]., Version: 2022-11-01., NOAA GML., https://doi.org/10.15138/5R14-K382, 2022.

Arnold, T., Rennick, C., O'Doherty, S., Say, D., Young, D., Stavert, A., and Wenger, A.: Deriving Emissions related to Climate Change Network: CO2, CH4, N2O, SF6 and CO measurements from Heathfield Tall Tower, East Sussex. Centre for Environmental Data Analysis, https://catalogue.ceda.ac.uk/uuid/df502fe4715c4177ab5e4e367a99316b, last accessed: 2024-02-1, 2019.

CEDA: World Data Centre for Greenhouse Gases, https://archive.ceda.ac.uk//, last accessed: 2023-09-10, 2023.

Cui, Z., Li, Y., Xiao, S., Tian, S., Tang, J., Hao, Y., and Zhang, X.: Recent progresses, challenges and proposals on SF6 emission reduction approaches, Science of The Total Environment, p. 167347, https://doi.org/10.1016/j.scitotenv.2023.167347, 2024.

DEFRA: Magnesium smelting: bans on use of sulphur hexafluoride. Department for Environment, Food Rural Affairs and Environment Agency (DEFRA), UK, December, https://www.gov.uk/guidance/magnesium-smelting-bans-on-use-of-sulphur-hexafluoride, last accessed: 2024-02-15, 2014.

di Sarra, A., Hall, B. D., Dylag, C., Couret, C., Lunder, C., Sweeney, C., Sferlazzo, D., Say, D., Mondeel, D. J., Young, D., Dlugokencky, E., Cuevas, E., Meinhardt, F., Technos, G. E., Dutton, G. S., Lee, H., Nance, J. D., Arduini, J., Pitt, J., Tsuboi, K., Stanley, K., Gatti, L. V., Steinbacher, M., Vollmer, M., Krummel, P., Rivas, P., Weiss, R. F., Wang, R., Chiavarini, S., Piacentino, S., O'Doherty, S., Reimann, S., A. Montzka, S., Saito, T., and Lan, X.: All SF6 data contributed to WDCGG by GAW stations and mobiles by 2022-09-05, https://doi.org/10.50849/WDCGG_SF6_ALL_2022, 2022.

Dlugokencky, E., Crotwell, A., Mund, J., Crotwell, M., and Thoning, K.: Atmospheric Sulfur Hexafluoride Dry Air Mole Fractions from the NOAA GML Carbon Cycle Cooperative Global Air Sampling Network, 1997-2019, Version: 2020-07, https://doi.org/10.15138/p646-pa37, 2020.

Doxsey-Whitfield, E., MacManus, K., Adamo, S. B., Pistolesi, L., Squires, J., Borkovska, O., and Baptista, S. R.: Taking advantage of the improved availability of census data: a first look at the gridded population of the world, version 4, Papers in Applied Geography, 1, 226–234, https://doi.org/10.1080/23754931.2015.1014272, 2015.

Dutton, G. and Hall, B.: Global Atmospheric Sulfur hexaflouride Dry Air Mole Fractions from the NOAA GML Halocarbons in situ Network, 1998-2023, Version: 2023-04-13, https://doi.org/10.7289/V5X0659V, 2023.

D'Amelio, M. T., Gatti, L. V., Martins, E. A. J., Polakiewicz, L., Miller, J., Crotwell, A., and Tans, P.: Greenhouse gases study in the Amazonia atmosphere, https://www.researchgate.net/profile/Luciana-Gatti/publication/242072841_GREENHOUSE_GASES_STUDY_IN_THE_AMAZONIA_ATMOSPHERE/links/0f3175375e48855b32000000/GREENHOUSE-GASES-STUDY-IN-THE-AMAZONIA-ATMOSPHERE.pdf, last accessed: 2024-02-01, 2024.

EC-JRC: GHS-POP R2015A - GHS population grid, derived from GPW4, multitemporal (1975, 1990, 2000, 2015). European Commission, Joint Research Centre (JRC) [Dataset] PID:, http://data.europa.eu/89h/jrc-ghsl-ghs_pop_gpw4_globe_r2015a, 2015.

Elkins, J. and Dutton, G.: Nitrous oxide and sulfur hexafluoride [in 'State of the Climate in 2008']. Bull. Amer. Meteor. Soc, 90 S38-S39, 2008.

Elkins, J. W., Moore, F., Hintsa, E., Hurst, D., Hall, B., Montzka, S., Miller, B., Dutton, G., and Nance, D.: HATS Airborne Projects, www.esrl.noaa.gov/gmd/hats/airborne/, last accessed: 2024-02-1, 2020.

Fahey, D. W., Churnside, J. H., Elkins, J. W., Gasiewski, A. J., Rosenlof, K. H., Summers, S., Aslaksen, M., Jacobs, T. A., Sellars, J. D., Jennison, C. D., et al.: Altair unmanned aircraft system achieves demonstration goals, Eos, Transactions American Geophysical Union, 87, 197–201, https://doi.org/10.1029/2006EO200002, 2006.

Fang, X., Hu, X., Janssens-Maenhout, G., Wu, J., Han, J., Su, S., Zhang, J., and Hu, J.: Sulfur hexafluoride (SF6) emission estimates for China: an inventory for 1990–2010 and a projection to 2020, Environmental science & technology, 47, 3848–3855, https://doi.org/10.1021/es304348x, 2013.

Gambhir, A., Napp, T., Hawkes, A., Höglund-Isaksson, L., Winiwarter, W., Purohit, P., Wagner, F., Bernie, D., and Lowe, J.: The contribution of non-CO2 greenhouse gas mitigation to achieving long-term temperature goals, Energies, 10, 602, https://doi.org/10.3390/en10050602, 2017.

Gensch, I. V., Bunz, H., Baumgardner, D., Christensen, L. E., Fahey, D. W., Herman, R. L., Popp, P. J., Smith, J. B., Troy, R. F., Webster, C. R., et al.: Supersaturations, microphysics and nitric acid partitioning in a cold cirrus cloud observed during CR-AVE 2006: an observation–modelling intercomparison study, Environmental research letters, 3, 035 003, https://doi.org/10.1088/1748-9326/3/3/035003, 2008.

Gomez-Pelaez, A. and Ramos, R.: 4.1 Installation of a New Gas Chromatograph at Izaña GAW Station (Spain) to Measure CH4, N2O, and SF6, GAW Report No. 186, p. 55, https://citeseerx.ist.psu.edu/document?repid=rep1&type=pdf&doi=0f54fc63d0aaa54c6146cba55cc0ba7bbfbad00f#page=73, 2009.

Gschrey, B., Behringer, D., Kleinschmidt, J., Jörß, W., Liste, V. ., Ludig, S., Wissner, N., Birchby, D., Dubey, J., and Hekman, J.: Support contract for an Evaluation and Impact Assessment for amending Regulation (EU) No 517/2014 on fluorinated greenhouse gases, CLIMA.A2/ETU/2019/0016, Impact Assessment Final Report, March, 2022.

Guillevic, M., Vollmer, M. K., Wyss, S. A., Leuenberger, D., Ackermann, A., Pascale, C., Niederhauser, B., and Reimann, S.: Dynamic–gravimetric preparation of metrologically traceable primary calibration standards for halogenated greenhouse gases, Atmospheric Measurement Techniques, 11, 3351–3372, https://doi.org/10.5194/amt-11-3351-2018, 2018.

Hall, B., Dutton, G., Mondeel, D., Nance, J., Rigby, M., Butler, J., Moore, F., Hurst, D., and Elkins, J.: Improving measurements of SF 6 for the study of atmospheric transport and emissions, Atmospheric Measurement Techniques, 4, 2441–2451, https://doi.org/10.5194/amt-4-2441-2011, 2011.

IPCC/TEAP: IPCC/TEAP Special Report on Safeguarding the Ozone Layer and the Global Climate System: Issues Related to Hydrofluorocarbons and Perfluorocarbons, Intergovernmental Panel on Climate Change (IPCC) and Technology and Economic Assessment Panel (TEAP), Cambridge University Press, Cambridge, United Kingdom and New York, USA, 2005.

Jensen, E., Pan, L. L., Honomichl, S., Diskin, G. S., Krämer, M., Spelten, N., Günther, G., Hurst, D. F., Fujiwara, M., Vömel, H., et al.: Assessment of observational evidence for direct convective hydration of the lower stratosphere, Journal of Geophysical Research: Atmospheres, 125, e2020JD032 793, https://doi.org/10.1029/2020JD032793, 2020.

Jensen, E. J., Pfister, L., Jordan, D. E., Fahey, D. W., Newman, P. A., Thornberry, T., Rollins, A., Diskin, G., Bui, T. P., McGill, M., et al.: The NASA Airborne Tropical TRopopause EXperiment (ATTREX), SPARC Newsletter, 41, 15–24, 2013.

Kim, J., Li, S., Mühle, J., Stohl, A., Kim, S.-K., Park, S., Park, M.-K., Weiss, R. F., and Kim, K.-R.: Overview of the findings from measurements of halogenated compounds at Gosan (Jeju Island, Korea) quantifying emissions in East Asia, Journal of Integrative Environmental Sciences, 9, 71–80, https://doi.org/10.1080/1943815X.2012.696548, 2012.

Krummel, P., Montzka, S., Harth, C., Miller, B., Mühle, J., Dlugokencky, E., Salameh, P., Hall, B., O'Doherty, S., Steele, L., Dutton, G., Young, D., Nance, J., Langenfelds, R., Elkins, J., Loh, Z., Lunder, C., Fraser, P., Derek, N., Mitrevski, B., Weiss, R., and Prinn, R.: An update of comparisons of non-CO2 trace gas measurements between AGAGE and NOAA at common sites, Presenta-

tion at the 19th WMO/IAEA GGMT Meeting, 28-31 Aug 2017, Empa, Dübendorf, Switzerland, https://community.wmo.int/en/meetings/ 19th-wmoiaea-meeting-carbon-dioxide-other-greenhouse-gases-and-related-measurement-techniques-ggmt-2017, last accessed: 2024-02-01, 2017.

195 Lan, X., Mund, J., Crotwell, A., Crotwell, M., Moglia, E., Madronich, M., Neff, D., and Thoning, K.: Atmospheric Sulfur Hexafluoride Dry Air Mole Fractions from the NOAA GML Carbon Cycle Cooperative Global Air Sampling Network, 1997-2022, Version: 2023-08-28, https://doi.org/10.15138/p646-pa37, 2023.

Loeffel, S., Eichinger, R., Garny, H., Reddmann, T., Fritsch, F., Versick, S., Stiller, G., and Haenel, F.: The impact of sulfur hexafluoride (SF_6) sinks on age of air climatologies and trends, Atmospheric Chemistry and Physics, 22, 1175–1193, https://doi.org/10.5194/acp-22-1175-2022, 2022.

200 Maione, M., Giostra, U., Arduini, J., Furlani, F., Graziosi, F., Vullo, E. L., and Bonasoni, P.: Ten years of continuous observations of stratospheric ozone depleting gases at Monte Cimone (Italy)—Comments on the effectiveness of the Montreal Protocol from a regional perspective, Science of the total environment, 445, 155–164, https://doi.org/10.1016/j.scitotenv.2012.12.056, 2013.

McKain, K., Sweeney, C., Baier, B., Crotwell, A., Crotwell, M., Handley, P., Higgs, J., Legard, T.and Madronich, M., Miller, J. B., Moglia, E.and Mund, J. N. D., Newberger, T., Wolter, S., and Laboratory, N. G. M.: NOAA Global Greenhouse Gas Reference Network Flask-

205 Air PFP Sample Measurements of CO2, CH4, CO, N2O, H2, SF6 and isotopic ratios collected from aircraft vertical profiles [Data set]. Version: 2022-12-01, https://doi.org/10.15138/39HR-9N34, 2022.

Newman, P., Fahey, D., and Global Hawk Pacific Experiment Science Team and others: The Global Hawk Pacific Mission (April-May, 2010), in: AGU Fall Meeting Abstracts, vol. 2010, pp. A53H–08, 2010.

NOAA Carbon Cycle Group ObsPack Team: Multi-laboratory compilation of atmospheric sulfure hexafluoride data for the

210 period 1983-2017; obspacksf61v2.1.12018−08−17; NOAA Earth System Research Laboratory, Global Monitoring Division, https://doi.org/10.15138/g3ks7p, 2018.

NOAA ESRL: NOAA Earth System Research Laboratoriy: Sulfur Hexafluoride (SF6) WMO Scale, https://gml.noaa.gov/ccl/sf6_scale.html, last accessed: 2022-05-27, 2014.

O'Doherty, S., Say, D., Stanley, K., Young, D., Pitt, J., and Wenger, A.: Deriving Emissions related to Climate Change Network: CO2, CH4,

215 N2O, SF6 and CO measurements from Bilsdale Tall Tower, North York Moors National Park. Centre for Environmental Data Analysis, https://catalogue.ceda.ac.uk/uuid/d2090552c8fe4c16a2fd7d616adc2d9f, last accessed: 2024-02-1, 2019.

Owens, J., Xiao, A., Bonk, J., DeLorme, M., and Zhang, A.: Recent development of two alternative gases to SF6 for high voltage electrical power applications, Energies, 14, 5051, https://doi.org/10.3390/en14165051, 2021.

Petropavlovskikh, I., Froidevaux, L., Shetter, R., Hall, S., Ullmann, K., Bhartia, P., Kroon, M., and Levelt, P.: In-flight validation of Aura MLS

220 ozone with CAFS partial ozone columns, Journal of Geophysical Research: Atmospheres, 113, https://doi.org/10.1029/2007JD008690, 2008.

Popa, M., Gloor, M., Manning, A., Jordan, A., Schultz, U., Haensel, F., Seifert, T., and Heimann, M.: Measurements of greenhouse gases and related tracers at Bialystok tall tower station in Poland, Atmospheric Measurement Techniques, 3, 407–427, https://doi.org/10.5194/amt-3-407-2010, 2010.

225 Prinn, R. G., Weiss, R. F., Arduini, J., Arnold, T., DeWitt, H. L., Fraser, P. J., Ganesan, A. L., Gasore, J., Harth, C. M., Hermansen, O., Kim, J., Krummel, P. B., Li, S., Loh, Z. M., Lunder, C. R., Maione, M., Manning, A. J., Miller, B. R., Mitrevski, B., Mühle, J., O'Doherty, S., Park, S., Reimann, S., Rigby, M., Saito, T., Salameh, P. K., Schmidt, R., Simmonds, P. G., Steele, L. P., Vollmer, M. K., Wang, R. H., Yao,

B., Yokouchi, Y., Young, D., and Zhou, L.: History of chemically and radiatively important atmospheric gases from the Advanced Global Atmospheric Gases Experiment (AGAGE), Earth System Science Data, 10, 985–1018, https://doi.org/10.5194/essd-10-985-2018, 2018.

230 Purohit, P. and Höglund-Isaksson, L.: Global emissions of fluorinated greenhouse gases 2005–2050 with abatement potentials and costs, Atmospheric Chemistry and Physics, 17, 2795–2816, https://doi.org/10.5194/acp-17-2795-2017, 2017.

Rust, D., Katharopoulos, I., Vollmer, M. K., Henne, S., O'doherty, S., Say, D., Emmenegger, L., Zenobi, R., and Reimann, S.: Swiss halocarbon emissions for 2019 to 2020 assessed from regional atmospheric observations, Atmospheric Chemistry and Physics, 22, 2447–2466, https://doi.org/10.5194/acp-22-2447-2022, 2022.

235 Saikawa, E., Rigby, M., Prinn, R. G., Montzka, S. A., Miller, B. R., Kuijpers, L. J. M., Fraser, P. J. B., Vollmer, M. K., Saito, T., Yokouchi, Y., Harth, C. M., Mühle, J., Weiss, R. F., Salameh, P. K., Kim, J., Li, S., Park, S., Kim, K.-R., Young, D., O'Doherty, S., Simmonds, P. G., McCulloch, A., Krummel, P. B., Steele, L. P., Lunder, C., Hermansen, O., Maione, M., Arduini, J., Yao, B., Zhou, L. X., Wang, H. J., Elkins, J. W., and Hall, B.: Global and regional emission estimates for HCFC-22, Atmospheric Chemistry and Physics, 12, 10 033–10 050, https://doi.org/10.5194/acp-12-10033-2012, 2012.

240 Saito, T.: private communication, feb. 05, 2021.

Salawitch, R., Canty, T., Avery, M., Wennberg, P., Team, T. S., et al.: Chemistry Observations from TC4: Overview, in: AGU Spring Meeting Abstracts, vol. 2008, pp. A53B–07, 2008.

Schauffler, S., Atlas, E., Lueb, R., Hendershot, R., and Pope, L.: Whole Air Sampler measurements of organic halogens in the troposphere and lower stratosphere from aircraft and balloon platforms., in: EGU General Assembly Conference Abstracts, p. 2991, 2010.

245 Schuck, T. and Obersteiner, F.: IAGOS-CARIBIC whole air sampler data (2024.01.12) [Data set]. Zenodo., https://doi.org/10.5281/zenodo.10495039, 2024.

Schwarz, W. and Leisewitz, A.: Emissions and reduction potentials of hydrofluorocarbons, perfluorocarbons and sulphur hexafluoride in Germany, Öko-Recherche, Frankfurt, Report for the German Federal Environmental Agency (Umweltbundesamt, UBA, Berlin), https://www.oekorecherche.de/sites/default/files/publikationen/f-gases.pdf, last accessed: 2024-02-15, 1999.

250 Simmonds, P. G., Rigby, M., Manning, A. J., Park, S., Stanley, K. M., McCulloch, A., Henne, S., Graziosi, F., Maione, M., Arduini, J., Reimann, S., Vollmer, M. K., Mühle, J., O'Doherty, S., Young, D., Krummel, P. B., Fraser, P. J., Weiss, R. F., Salameh, P. K., Harth, C. M., Park, M.-K., Park, H., Arnold, T., Rennick, C., Steele, L. P., Mitrevski, B., Wang, R. H. J., and Prinn, R. G.: The Increasing Atmospheric Burden of the Greenhouse Gas Sulfur Hexafluoride (SF6), Atmospheric Chemistry and Physics, 20, 7271–7290, https://doi.org/10.5194/acp-20-7271-2020, 2020.

255 Stavert, A. R., O'doherty, S., Stanley, K., Young, D., Manning, A. J., Lunt, M. F., Rennick, C., and Arnold, T.: UK greenhouse gas measurements at two new tall towers for aiding emissions verification, Atmospheric Measurement Techniques, 12, 4495–4518, https://doi.org/710.5194/amt-12-4495-2019, 2019.

Stiller, G., Harrison, J. J., Haenel, F., Glatthor, N., and Kellmann, S.: MIPAS monthly zonal mean Age of Air data, based on MIPAS SF6 retrievals, processed at KIT-IMK, Karlsruhe, https://doi.org/10.5445/IR/1000139453, 2021.

260 Tohjima, Y., Machida, T., Utiyama, M., Katsumoto, M., Fujinuma, Y., and Maksyutov, S.: Analysis and presentation of in situ atmospheric methane measurements from Cape Ochi-ishi and Hateruma Island, Journal of Geophysical Research: Atmospheres, 107, ACH–8, https://doi.org/10.1029/2001JD001003, 2002.

Tohka, A.: The GAINS Model for Greenhouse Gases – Version 1.0: HFC, PFC and SF6, International Institute for Applied Systems Analysis (IIASA), Laxenburg, Austria, October, 2005.

Tørseth, K., Aas, W., Breivik, K., Fjæraa, A. M., Fiebig, M., Hjellbrekke, A.-G., Lund Myhre, C., Solberg, S., and Yttri, K. E.: Introduction to the European Monitoring and Evaluation Programme (EMEP) and observed atmospheric composition change during 1972–2009, Atmospheric Chemistry and Physics, 12, 5447–5481, https://doi.org/10.5194/acp-12-5447-2012, 2012.

UNFCCC: National Inventory Submissions 2023, https://unfccc.int/ghg-inventories-annex-i-parties/2023, 2023.

USGS: Magnesium Statistics and Information, United States Geological Survey (USGS), https://www.usgs.gov/centers/national-minerals-information-center/magnesium-statistics-and-information, 2023.

Waugh, D. and Hall, T.: Age of stratospheric air: Theory, observations, and models, Reviews of Geophysics, 40, 1–1, https://doi.org/10.1029/2000RG000101, 2002.

Wiegmans, B.: GridKit extract of ENTSO-E interactive map, Zenodo: Oldenburg, Germany, https://doi.org/10.5281/zenodo.55853, 2016.

Wofsy, S., Afshar, S., Allen, H., Apel, E., Asher, E., Barletta, B., Bent, J., Bian, H., Biggs, B., Blake, D., et al.: ATom: Merged atmospheric chemistry, trace gases, and aerosols, ORNL DAAC, Oak Ridge, Tennessee, USA, https://doi.org/10.3334/ORNLDAAC/1581, 2018.

Wofsy, S. C.: HIAPER Pole-to-Pole Observations (HIPPO): fine-grained, global-scale measurements of climatically important atmospheric gases and aerosols, Philosophical Transactions of the Royal Society A: Mathematical, Physical and Engineering Sciences, 369, 2073–2086, https://doi.org/10.1098/rsta.2010.0313, 2011.

Zellweger, C., Klausen, J., and Buchmann, B.: System and performance audit for surface ozone, carbon monoxide and methane at the global GAW station Zugspitze-Schneefernerhaus Germany, June, 2006. Dübendorf, Switzerland: EMPA. WCC-Empa Report 06/4, https://citeseerx.ist.psu.edu/document?repid=rep1&type=pdf&doi=49d2b76db4ad0b715ed94cb859feba895d81a4b1, last accessed: 2024-02-1, 2020.

Zhou, S., Teng, F., and Tong, Q.: Mitigating sulfur hexafluoride (SF6) emission from electrical equipment in China, Sustainability, 10, 2402, https://doi.org/10.3390/su10072402, 2018.